Supplementary Information (SI) for Chemical Communications.
This journal is © The Royal Society of Chemistry 2025

A new carborane scaffold for assembling metal–organic frameworks

Hunter J. Windsor,*[a] Thomas J. C. Carraro,[a] Robert J. Walwyn, [a] Louis M. Rendina [a,b] and Cameron J. Kepert *[a]

[a]School of Chemistry, The University of Sydney, New South Wales 2006, Australia.

[b]The University of Sydney Nano Institute (Sydney Nano), The University of Sydney, New South Wales 2006, Australia.

Email: hunter.windsor@sydney.edu.au

Email: cameron.kepert@sydney.edu.au

Contents

S1 – Experimental

S1.1 – General

All precursor chemicals were commercially available (Arctom, Sigma, Boron Specialties, Katchem) and were used without further purification. 4-Iodopyridine was prepared from a literature procedure.[1] Anhydrous THF was dried over activated 4 Å molecular sieves for at least 48 hours prior to use. All other solvents were used with any further purification. Column chromatography was carried out using Merck silica gel 60 (230–400 mesh) on a Biotage Selekt. Analytical thin layer chromatography (TLC) was performed using Merck TLC silica gel 60 F254 aluminium plates. Compounds were visualised under shortwave (254 nm) and/or longwave (365 nm) ultraviolet (UV) light. Carborane-containing compounds were visualised on TLC plates using an acidified aqueous $PdCl_2$ stain (1% $PdCl_2$ by mass in 1 M HCl) and the plates heated by means of a heat gun.

All ^{1}H, $^{11}B\{^{1}H\}$, and $^{13}C\{^{1}H\}$ NMR spectra were recorded at 300 K on a Bruker NEO 500 (^{1}H at 500 MHz, ^{11}B at 160 MHz, and ^{13}C at 125 MHz). All NMR signals are reported in ppm; ^{1}H and ^{13}C NMR signals were referenced to their residual solvent peaks as internal standards. $^{11}B\{^{1}H\}$ NMR spectra were referenced automatically by the spectrometer software (Bruker Topspin) according to the unified chemical shift scale *via* the lock frequency of the solvent. High-resolution mass spectra (HRMS) were obtained using a Bruker 7T Apex Qe Fourier Transform Ion-Cyclotron Resonance mass spectrometer (FT-ICR-MS) fitted with an Apollo II APCI source.

S1.2 – Syntheses

S1.2.1 – 1,12-bis(4-pyridyl)-*closo*-1,12-carborane (*p*-Py_2CB)

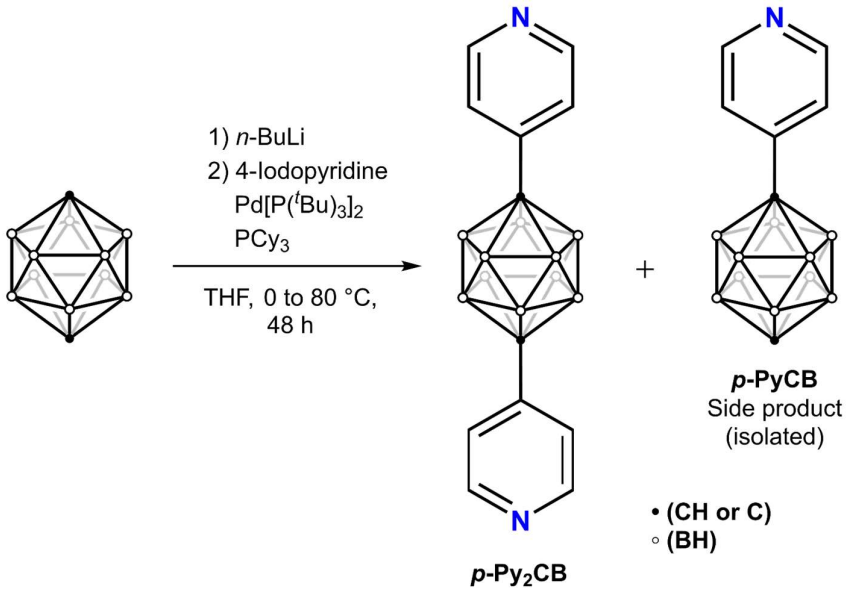

To a dry Schlenk flask of *closo*-1,12-carborane (0.050 g, 0.347 mmol, 1 eq.) in THF (4 mL) at 0 °C was added *n*-BuLi (1.6 M, 0.763 mmol, 0.47 mL, 2.2 eq.). The solution was kept at 0 °C with stirring for 0.5 h and was then heated to 50 °C for an additional 2 hours. $Pd[P(^tBu)_3]_2$ (5 mol %, 0.017 mmol, 0.0089 g), PCy_3 (10 mol %, 0.035 mmol, 0.0098 mg), and 4-iodopyridine (0.833 mmol, 0.171 g, 2.4 eq.) were then added under an inert nitrogen atmosphere, and the mixture was heated to reflux and monitored by TLC. After the reaction was completed (as determined by TLC), the reaction mixture was quenched by the addition of methanol (5 mL) and then dry loaded onto Celite filter-aid. The dry-loaded crude solid was then purified by silica gel column chromatography eluting with MeOH:DCM (1:99 *v/v* for mono substituted *p*-PyCB, 2:98 *v/v* for disubstituted *p*-Py_2CB, ramp *ca.* 20 column volumes). Fractions were combined and the solvents were evaporated *in vacuo*, and the resulting solid was washed several times with ether (5 × 5 mL) to afford the product as a colourless powder (0.082 g, 79%). Colourless block crystals suitable for X-ray diffraction were grown *via* slow evaporation from a MeOH:DCM (1:9 *v/v*) mixture.

^{1}H NMR (500 MHz, $CDCl_3$): δ 8.46 (d, br, 4H, $^3J_{H–H}$ = 6.41 Hz), 7.14 (d, br, 4H, $^3J_{H–H}$ = 6.38 Hz), 3.29–1.97 (m, 10H, B_{cage}–H).

^{11}B{^{1}H} (160 MHz, $CDCl_3$): δ −12.2 (s, 10B).

^{13}C{^{1}H} (125 MHz, $CDCl_3$): δ 149.9, 144.5, 121.9, 81.4.

Raman shift (cm^{-1}): *v* 3063, 2634, 2622, 2605, 2590, 1596, 1266, 1229, 1078, 1038, 996, 952, 905, 868, 794, 775, 715, 671, 605, 526, 357, 227, 128, 107.

HRMS (APCI): $[M + H]^+$ *m/z* calcd for $C_{12}H_{18}B_{10}N_2$: 299.25519; found: 299.25465.

S1.2.2 – 1-(4-pyridyl)-*closo*-1,12-carborane (*p*-PyCB)

Isolated as an by-product from the synthesis of *p*-Py_2CB as a colourless powder (12 mg, 16%). Colourless block crystals suitable for X-ray diffraction were grown *via* slow evaporation from a MeOH:DCM (1:9 *v/v*) mixture.

^{1}H NMR (500 MHz, $CDCl_3$): δ 8.48 (d, br, 2H, $^{3}J_{H–H}$ = 6.29 Hz), 7.22 (d, br, 2H, $^{3}J_{H–H}$ = 6.29 Hz), 3.58 (s, br, 1H, C_{cage}–H), 3.05–1.80 (m, 10H, B_{cage}–H).

^{11}B{^{1}H} NMR (160 MHz, $CDCl_3$): δ −12.8 (s, 5B), −14.7 (s, 5B).

^{13}C{^{1}H} NMR (125 MHz, $CDCl_3$): δ 150.0, 144.4, 121.5, 61.6, (C_{cage}–C not observed).

Raman shift (cm^{-1}): *v* 3075, 3018, 2632, 2622, 2603, 1637, 1598, 1501, 1394, 1262, 1228, 1075, 1037, 998, 946, 904, 795, 771, 745, 680, 606, 540, 327, 282, 116, 84, 71.

HRMS (APCI): $[M + H]^+$ *m/z* calcd for $C_7H_{15}B_{10}N$: 222.22840; found: 222.22797.

S1.2.3 – 1,7-bis(4-pyridyl)-*closo*-1,7-carborane (*m*-Py_2CB)

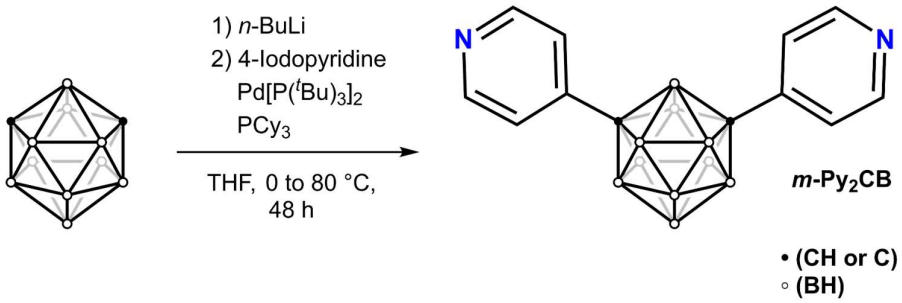

To a dry Schlenk flask of *closo*-1,7-carborane (0.050 g, 0.347 mmol, 1 eq.) in THF (4 mL) at 0 °C was added *n*-BuLi (1.6 M, 0.763 mmol, 0.47 mL, 2.2 eq.). The solution was kept at 0 °C with stirring for 0.5 h and was then heated to 50 °C for an additional 2 hours. $Pd[P(^tBu)_3]_2$ (5 mol %, 0.017 mmol, 0.0089 g), PCy_3 (10 mol %, 0.035 mmol, 0.0098 mg), and 4-iodopyridine (0.833 mmol, 0.171 g, 2.4 eq.) were then added under an inert nitrogen atmosphere, and the mixture was heated to reflux and monitored by TLC. After the reaction was completed (as determined by TLC), the reaction mixture was quenched by the addition of methanol (5 mL) and then dry loaded onto Celite filter-aid. The dry-loaded crude solid was then purified by silica gel column chromatography eluting with MeOH:DCM (2:98 *v/v*). Fractions were combined and the solvent evaporated in *vacuo* to afford the product as a colourless powder (0.064 g, 62%). Colourless block crystals suitable for X-ray diffraction were grown *via* slow evaporation from a MeOH:DCM (1:9 *v/v*) mixture.

^{1}H NMR (500 MHz, acetone-d_6): δ 8.46 (d, br, 4H, $^{3}J_{H–H}$ = 6.38 Hz), 7.14 (d, br, 4H, $^{3}J_{H–H}$ = 6.29 Hz) 3.29–1.97 (m, 10H, B_{cage}–H).

^{11}B{^{1}H} NMR (160 MHz, acetone-d_6): δ −4.9 (s, 2B), −9.6 (s, 6B), −13.5 (s, 2B).

^{13}C{^{1}H} NMR (125 MHz, acetone-d_6): δ 150.8, 144.0, 123.5, 77.3.

Raman shift (cm^{-1}): *v* 3060, 3046, 2681, 2669, 2652, 2642, 2631, 2615, 2601, 2590, 2572, 2561, 1595, 1268, 1229, 1060, 997, 774, 661, 608, 592, 575, 512, 290, 266, 244, 171, 140, 107.

HRMS (APCI): $[M + H]^+$ *m/z* calcd for $C_{12}H_{18}B_{10}N_2$: 299.25519; found: 299.25500.

S1.2.4 – [Zn(*p*-Py_2CB)(bdc)]·DMF (**ZnCB-1**)

p-Py_2CB (11.5 mg, 38.5 μmol) and 1,4-benzenedicarboxylic acid (H_2bdc) (6.40 mg, 38.5 μmol) were added to a 21 mL glass scintillation vial, with zinc(II) nitrate hexahydrate (11.5 mg, 38.5 μmol) being added to a separate 21 mL vial. *N*,*N*-dimethylformamide (DMF) (3 mL) was added to each vial. The vials were heated to 120 °C and, after complete dissolution of reagents (assisted by means of sonication), the vial containing the zinc(II) nitrate hexahydrate solution was transferred by syringe to the vial containing the dipyridyl and dicarboxylic acid solution. The vial containing the resulting colourless solution was capped and heated in an aluminium heat block at 120 °C for 18–24 h to afford colourless rectangular prismatic crystals of **ZnCB-1**. Yield: 11 mg (69%).

Raman shift (cm^{-1}): *ν* 3082, 2930, 2633, 2610, 1677, 1652, 1615, 1496, 1437, 1410, 1260, 1170, 1141, 1076, 1026, 887, 800, 719, 662, 523, 296.

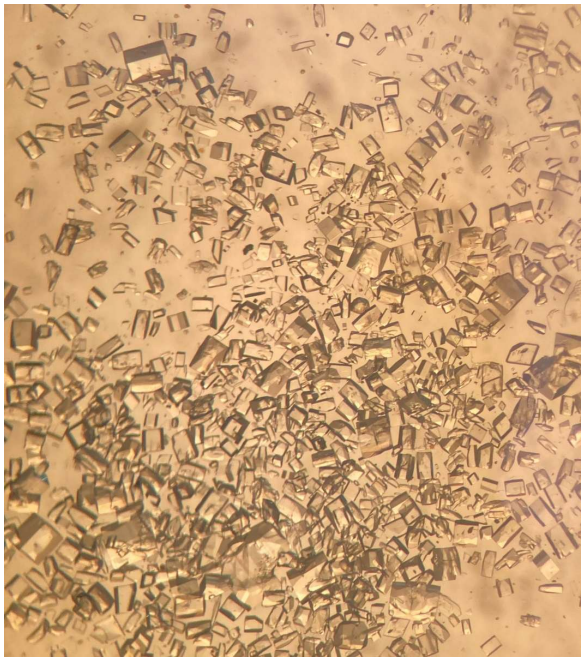

Figure S1 Image of **ZnCB-1** crystals prepared under solvothermal reaction conditions.

S2 – Single Crystal X-Ray Diffraction (SCXRD)

Single crystal X-ray data collections were performed using either a Rigaku XtaLAB Synergy-DW Custom diffractometer (FR-X rotating-anode source, Rigaku HyPix-6000HE detector) or an Agilent Technologies SuperNova (microfocus source, Atlas CCD detector), with both diffractometer sources outputting confocal mirror-monochromated Cu-Kα radiation (λ = 1.54184 Å). Data were collected about ω scans and then were integrated and reduced with absorption corrections (Gaussian grid face-indexed numerical integration with beam profile, or empirical based on equivalents) being applied using CrysAlisPro. Structure solutions were obtained by intrinsic phasing using SHELXT[2] and were refined by full-matrix least-squares on all unique F^2 values using SHELXL[3] as implemented within the OLEX2-1.5 GUI.[4] Molecular and crystal structure drawings were made using CrystalMaker 11 (version 11.1.2). The full details used in each refined X-ray structure can be found in the respective crystallographic information file (CIF) for each compound. It should be noted that the submitted CIFs for **ZnCB-1** include modelled DMF solvent. For consistency, the DMF was also treated by an Olex2 solvent mask to account for the contribution of DMF solvent molecules to the structure factors. The 150 K and 350 K data tables for **ZnCB-1** are given below (Table S1), while the other variable temperature datasets are freely accessible online.

ZnCB-1 (CCDC: 2449387 (150 K), 2449388 (160 K), 2449389 (170 K), 2449390 (180 K), 2449391 (190 K), 2449392 (200 K), 2449393 (210 K), 2449394 (220 K), 2449395 (230 K), 2449396 (240 K), 2449397 (250 K), 2449398 (260 K), 2449399 (270 K), 2449400 (280 K), 2449401 (290 K), 2449402 (300 K), 2449403 (310 K), 2449404 (320 K), 2449405 (330 K), 2449406 (340 K), 2449407 (350 K)).

p-Py_2CB (CCDC: 2449440)

m-Py_2CB (CCDC: 2449441)

p-PyCB (CCDC: 2449442)

The authors acknowledge the facilities and the scientific and technical assistance of Sydney Analytical, a core research facility at The University of Sydney.

Instrument funding acknowledgement: LIEF LE210100144

Table S1 Crystal data and structure refinement for **ZnCB-1** at 150 K and 350 K.

CCDC number	2449387	2449407
Empirical formula	$C_{17}H_{20}B_5N_2O_5Zn$	$C_{17}H_{20}B_5N_2O_5Zn$
Formula weight	451.77	451.77
Temperature (K)	150(2)	350(2)
Crystal system	monoclinic	monoclinic
Space group	*C*2/*c*	*C*2/*c*
a (Å)	18.7459(4)	18.7603(4)
b (Å)	13.1934(3)	13.4307(4)
c (Å)	17.3101(4)	17.1661(4)
β (°)	93.237(2)	91.022(2)
V (Å^3)	4274.34(17)	4324.55(19)
Z (*Z*')	8 (1)	8 (1)
ρ_{calc} (g cm^{-3})	1.404	1.388
μ (mm^{-1})	1.854	1.832
Absorption correction	Empirical from equivalents	Empirical from equivalents
F(000)	1848	1848
Crystal size (mm^3)	0.150 × 0.050 × 0.025	0.150 × 0.050 × 0.025
Radiation	Cu-K*α* (λ = 1.54184 Å)	Cu-K*α* (λ = 1.54184 Å)
2*Θ* range for data collection (°)	8.2 to 144.59	8.096 to 144.758
Index ranges	$-15 \le h \le 22$, $-16 \le k \le 15$, $-21 \le l \le 21$	$-22 \le h \le 15$, $-16 \le k \le 16$, $-20 \le l \le 21$
Reflections collected	20174	20018
Independent reflections	4131 [R_{int} = 0.0257, R_{sigma} = 0.0205]	4181 [R_{int} = 0.0268, R_{sigma} = 0.0259]
Data/restraints/parameters	4131/7/312	4181/145/358
Goodness-of-fit on F^2	1.068	1.061
Final *R* indexes [$I \ge 2\sigma(I)$]	R_1 = 0.0375, wR_2 = 0.1158	R_1 = 0.0387, wR_2 = 0.1143
Final *R* indexes [all data]	R_1 = 0.0418, wR_2 = 0.1194	R_1 = 0.0516, wR_2 = 0.1254
Largest diff. peak/hole (e Å^{-3})	1.07/−0.51	0.77/−0.33

Table S2 Crystal data and structure refinement for *p*-Py_2CB.

CCDC number	2449440
Empirical formula	$C_{12}H_{18}B_{10}N_2$
Formula weight	298.38
Temperature (K)	150(2)
Crystal system	monoclinic
Space group	$P2_1/c$
a (Å)	7.96970(10)
b (Å)	10.5301(2)
c (Å)	9.62270(10)
β (°)	106.1280(10)
V (Å^3)	775.77(2)
Z (Z')	2 (0.5)
ρ_{calc} (g cm^{-3})	1.277
μ (mm^{-1})	0.477
Absorption correction	Gaussian
F(000)	308
Crystal size (mm^3)	0.209 × 0.169 × 0.046
Radiation	Cu-Kα (λ = 1.54184 Å)
2Θ range for data collection (°)	11.558 to 144.984
Index ranges	$-9 \le h \le 9$, $-12 \le k \le 11$, $-11 \le l \le 11$
Reflections collected	12437
Independent reflections	1524 [R_{int} = 0.0257, R_{sigma} = 0.0149]
Data/restraints/parameters	1524/0/145
Goodness-of-fit on F^2	1.055
Final R indexes [$I \ge 2\sigma(I)$]	R_1 = 0.0358, wR_2 = 0.0999
Final R indexes [all data]	R_1 = 0.0372, wR_2 = 0.1014
Largest diff. peak/hole (e Å^{-3})	0.29/−0.22

Table S3 Crystal data and structure refinement for *m*-Py_2CB.

CCDC number	2449441
Empirical formula	$C_{12}H_{18}B_{10}N_2$
Formula weight	298.38
Temperature (K)	150(2)
Crystal system	monoclinic
Space group	$P2_1/c$
a (Å)	15.7644(3)
b (Å)	10.3772(2)
c (Å)	9.8017(2)
β (°)	96.299(2)
V (Å^3)	1593.78(5)
Z (Z')	4 (1)
ρ_{calc} (g cm^{-3})	1.244
μ (mm^{-1})	0.465
Absorption correction	Gaussian
F(000)	616
Crystal size (mm^3)	0.384 × 0.24 × 0.21
Radiation	Cu-Kα (λ = 1.54184 Å)
2Θ range for data collection (°)	5.64 to 144.588
Index ranges	$-18 \le h \le 19$, $-12 \le k \le 12$, $-12 \le l \le 11$
Reflections collected	14885
Independent reflections	3088 [R_{int} = 0.0208, R_{sigma} = 0.0138]
Data/restraints/parameters	3088/0/247
Goodness-of-fit on F^2	1.075
Final R indexes [$I \ge 2\sigma(I)$]	R_1 = 0.0353, wR_2 = 0.0931
Final R indexes [all data]	R_1 = 0.0364, wR_2 = 0.0941
Largest diff. peak/hole (e Å^{-3})	0.23/−0.20

Table S4 Crystal data and structure refinement for *p*-PyCB.

CCDC number	2449442
Empirical formula	$C_7H_{15}B_{10}N$
Formula weight	221.30
Temperature (K)	150(2)
Crystal system	orthorhombic
Space group	$Pna2_1$
a (Å)	14.5733(2)
b (Å)	11.9319(2)
c (Å)	7.21180(10)
V (Å^3)	1254.04(3)
Z (Z')	4 (1)
ρ_{calc} (g cm^{-3})	1.172
μ (mm^{-1})	0.391
Absorption correction	Gaussian
F(000)	456
Crystal size (mm^3)	0.449 × 0.067 × 0.016
Radiation	Cu-Kα (λ = 1.54184 Å)
2Θ range for data collection (°)	9.58 to 144.7
Index ranges	$-17 \le h \le 13$, $-14 \le k \le 14$, $-8 \le l \le 8$
Reflections collected	11633
Independent reflections	2346 [R_{int} = 0.0341, R_{sigma} = 0.0276]
Data/restraints/parameters	2346/1/164
Goodness-of-fit on F^2	1.038
Final R indexes [$I \ge 2\sigma(I)$]	R_1 = 0.0372, wR_2 = 0.0988
Final R indexes [all data]	R_1 = 0.0389, wR_2 = 0.1000
Largest diff. peak/hole (e Å^{-3})	0.17/−0.24
Flack parameter	0.1(5)

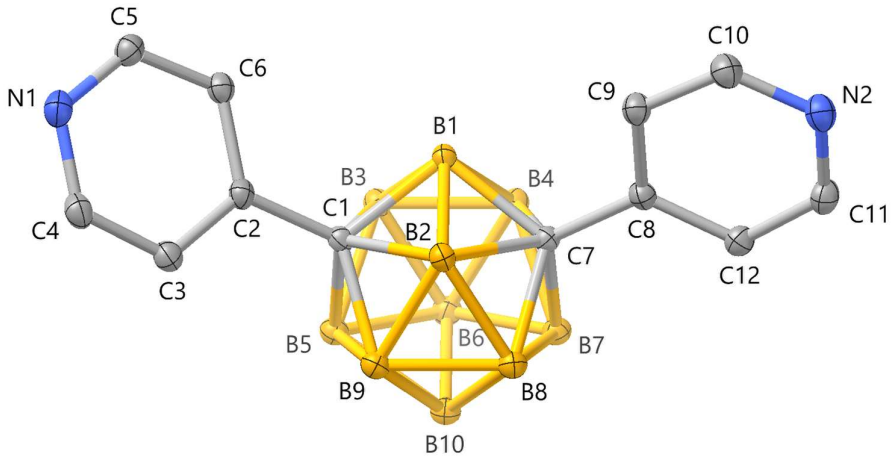

Figure S2 Molecular structure and asymmetric unit of *m*-Py_2CB with displacement ellipsoids drawn at the 50% probability level. Hydrogen atoms are omitted for clarity.

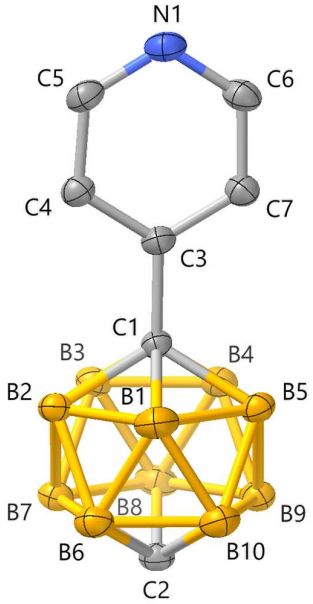

Figure S3 Molecular structure and asymmetric unit of *p*-PyCB with displacement ellipsoids drawn at the 50% probability level. Hydrogen atoms are omitted for clarity.

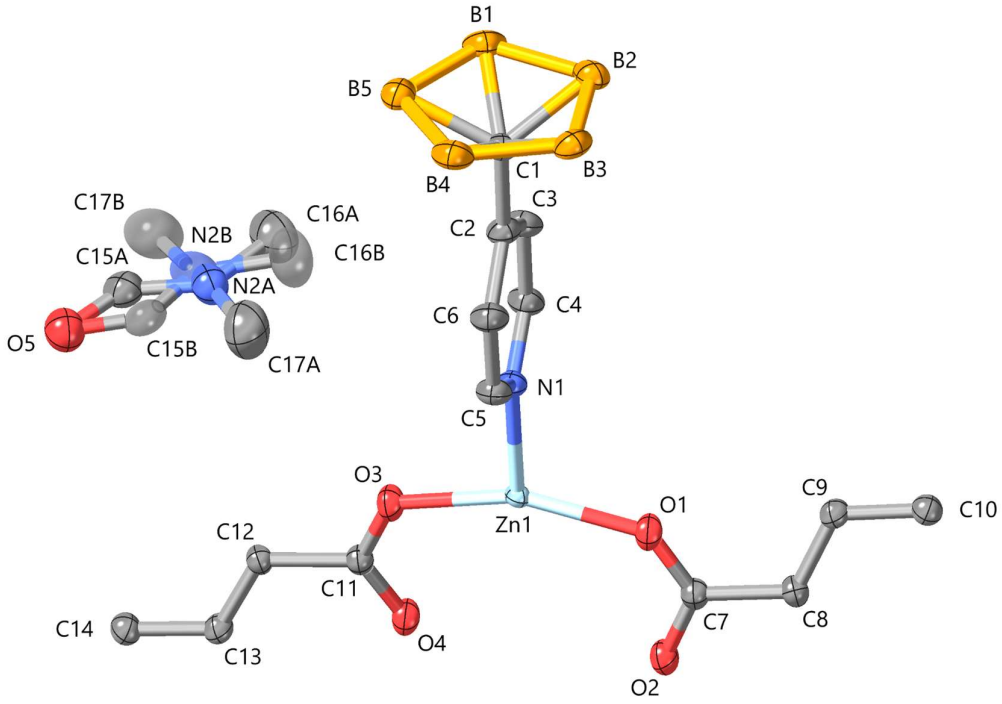

Figure S4 Asymmetric unit of **ZnCB-1** at 150 K with displacement ellipsoids drawn at the 50% probability level. Minor component of the disordered DMF solvent is shown transculent. Hydrogen atoms are omitted for clarity.

Figure S5 Single crystal of **ZnCB-1** at 300 K (left) and 380 K (right) after attempted desolvation, with the latter showing loss of translucency and monocrystallinity.

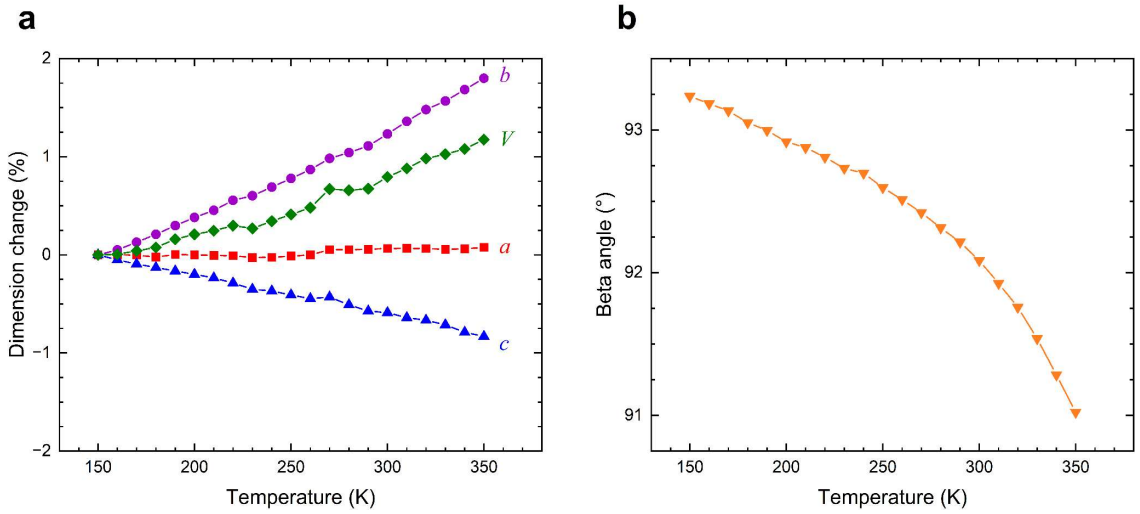

Figure S6 VT-SCXRD unit cell dimension changes of **ZnCB-1**. The percentage changes are given for the *a*, *b*, *c*, and volume parameters in (a), while the absolute change is given for the *β* angle in (b).

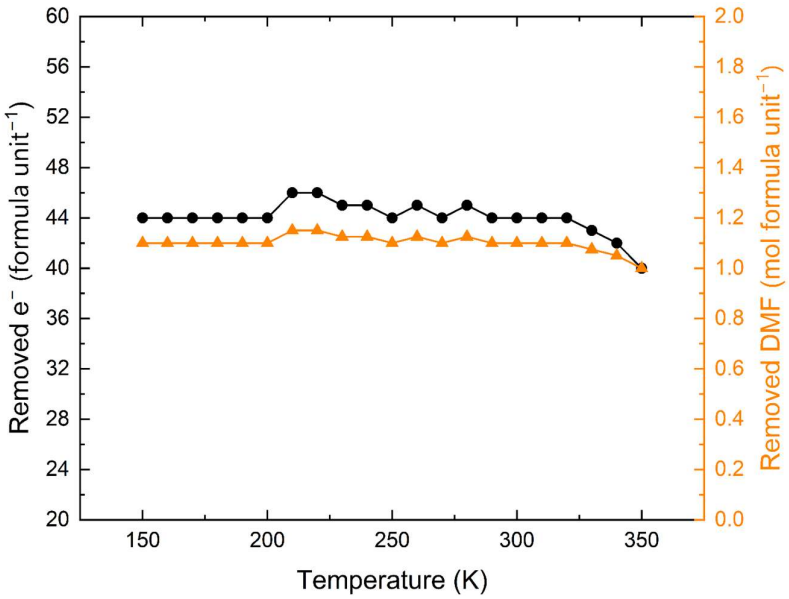

Figure S7 Olex2 solvent mask results from **ZnCB-1** VT-SCXRD datasets when not modelling the DMF molecule. The removed solvent mask electron density in **ZnCB-1** is consistent for an expected 1 mol DMF per formula unit (8 molecules per unit cell). The orange axis refers to the hypothetical corresponding amount of DMF removed per applied solvent mask per K. Some degree of guest desorption is evident prior to loss of monocrystallinity at *ca.* 380 K.

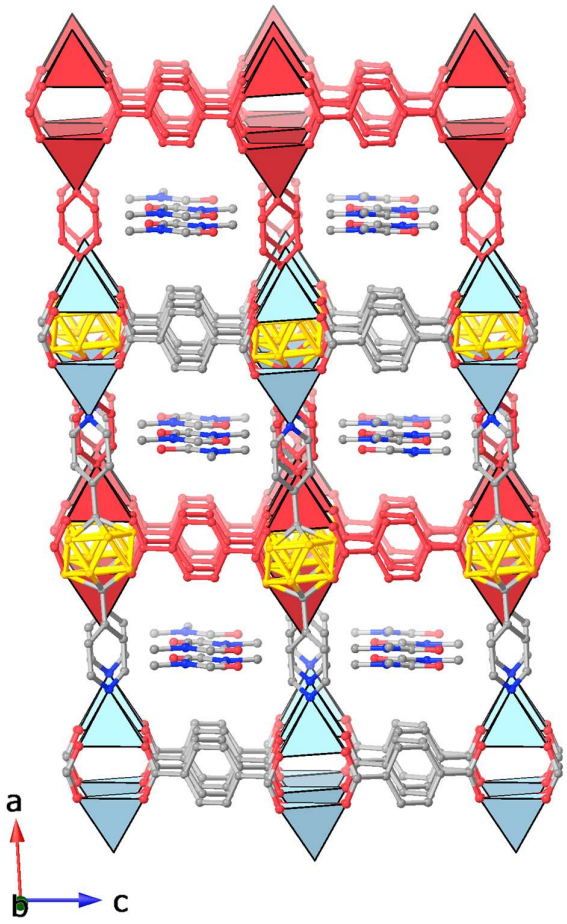

Figure S8 Packing structure of **ZnCB-1**, as viewed along the [010] direction and showing included pore DMF. The interpenetrating net is coloured red for clarity.

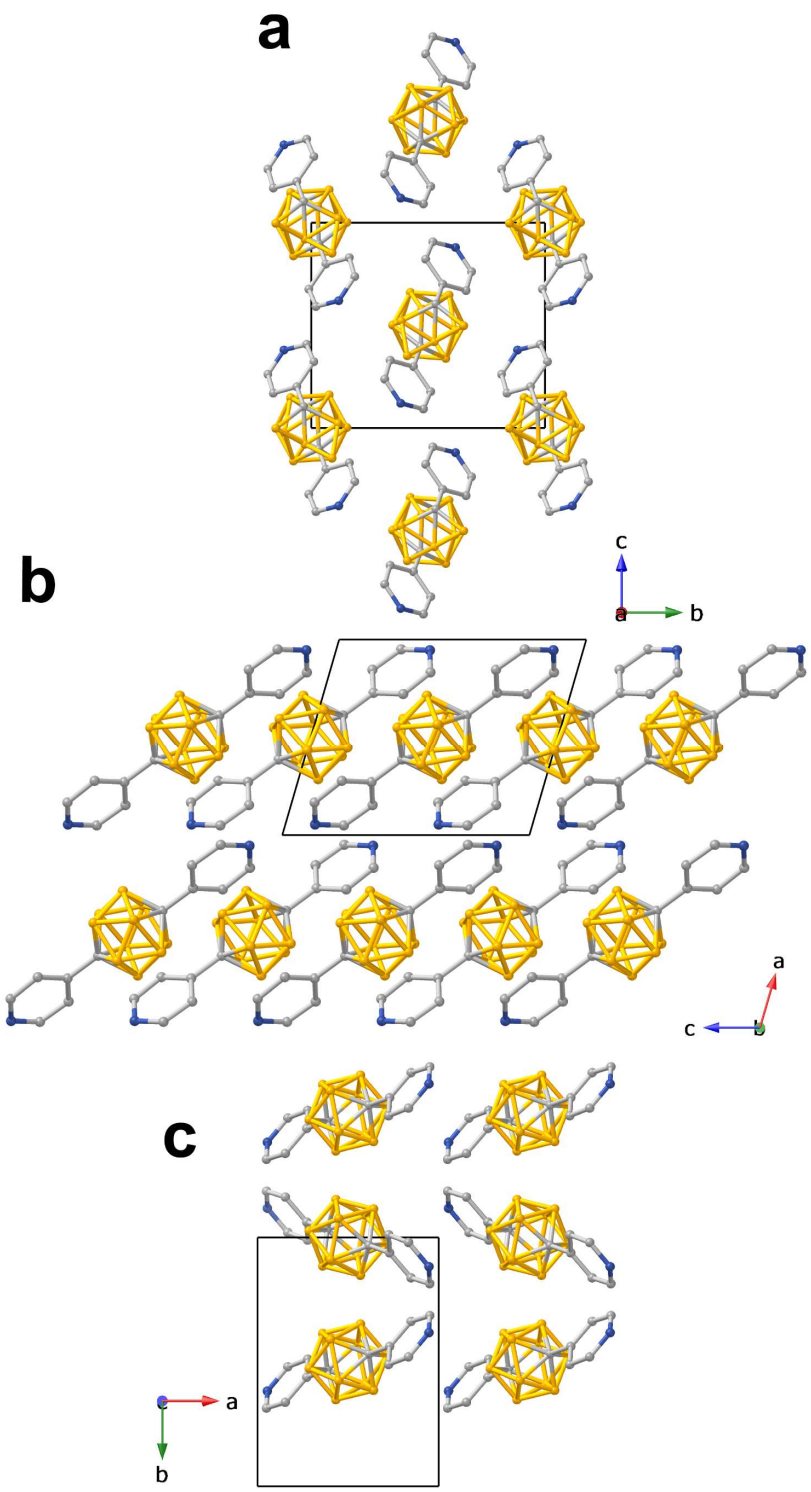

Figure S9 Packing structure of *p*-Py_2CB along the (a) [100], (b) [010], and (c) [001] directions.

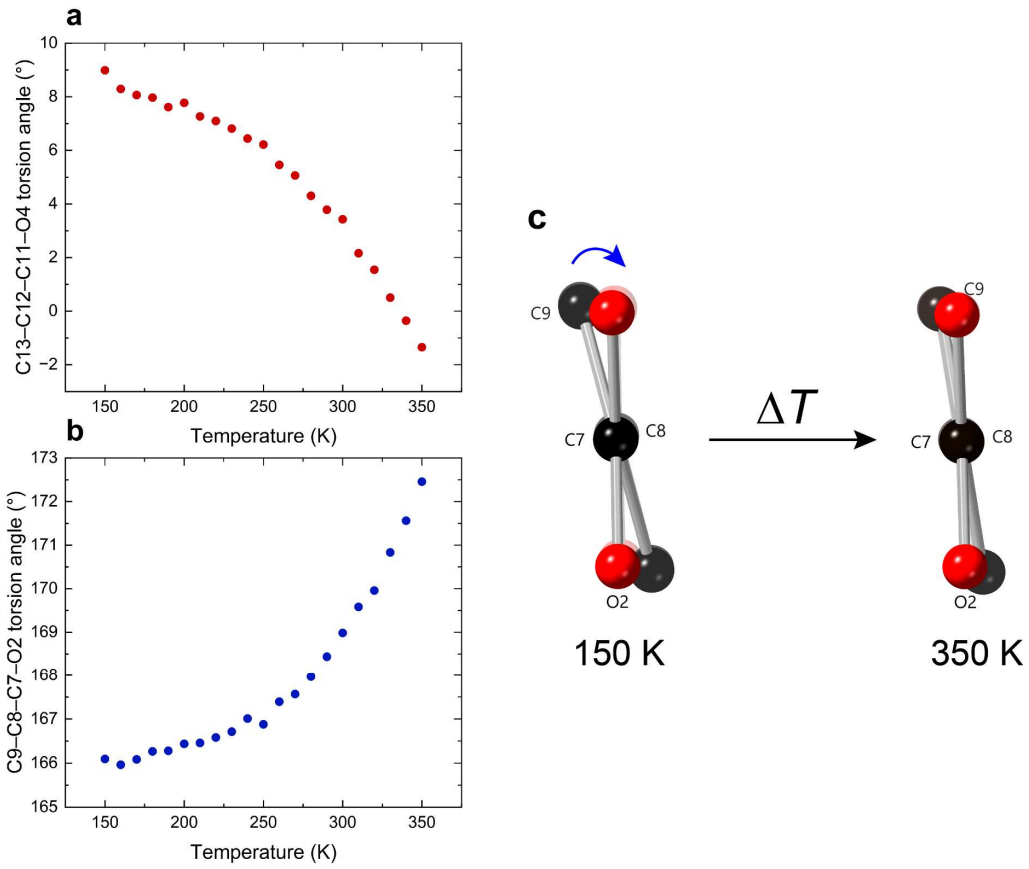

Figure S10 Crystallographically determined torsion angles as a function of temperature: (a) C9–C8–C7–O2, (b) C13–C12–C11–O4. (c) Structural visualisation of the C9–C8–C7–O2 torsion angle, as seen quantitatively in (b) between 150 K and 350 K in the bridging bdc ligand as viewed front on (blue arrow represents the direction of dihedral twist and motion of the benzene ring). The torsion angle approaches 180° with temperature, indicating that the plane defined by the carboxylate oxygens relative to that of the benzene ring approaches co-planarity.

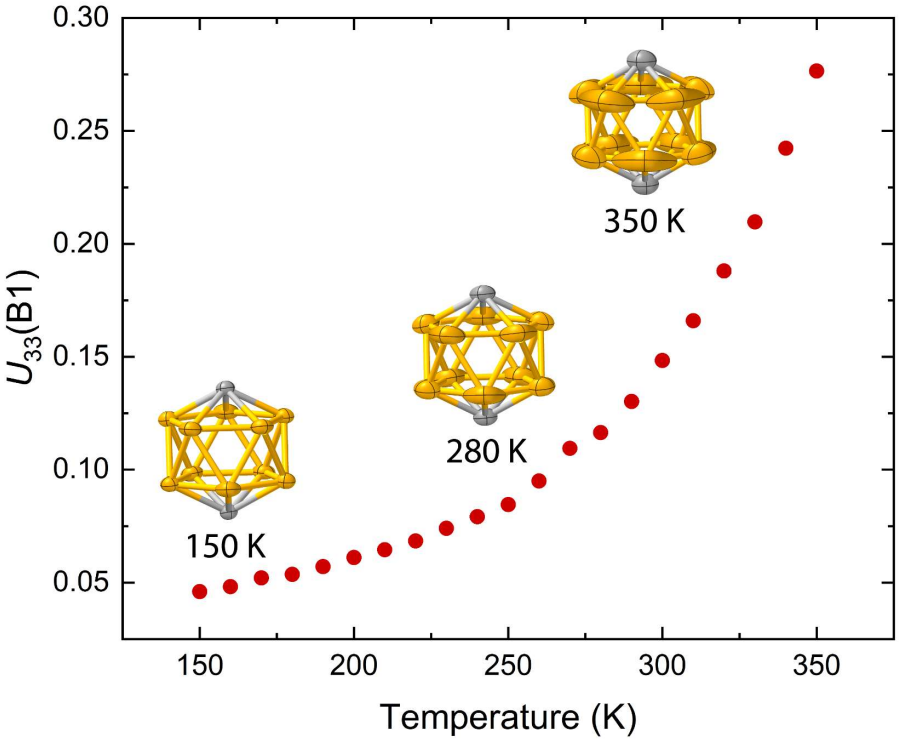

Figure S11 Crystallographically determined U_{33} displacement parameter for B1 in **ZnCB-1** as a function of temperature. B1 was taken as a representative example as all five inequivalent boron atoms exhibit the same temperature-dependence on their U_{33} displacement parameter. To generate this plot, no disorder modelling was performed on datasets 280 K and above, nor were any thermal restraints applied to the carborane residue. Inset figures: isolated carborane residue in **ZnCB-1** with displacement parameters drawn at the 50% probability level. Note: the deposited CIFs for temperatures 280 K and above include disorder modelling.

S3 – Powder X-Ray Diffraction (PXRD)

Single crystals of **ZnCB-1** were first washed with DMF (4 × 5 mL) to remove any residual ligand or metal salts and were then gently ground to produce a bulk polycrystalline sample before being loaded as a solid suspension in DMF into a 0.5 mm glass capillary. Centrifugation was applied to concentrate the powder before the capillary was flame-sealed to prevent solvent loss.

PXRD patterns were acquired by means of a PANalytical XPert Pro diffractometer operating in Debye-Scherrer geometry with monochromated Cu-Kα (λ = 1.540598 Å) radiation and a PIXcell1D detector, covering a 2θ range of 0–60°. Additional PXRD patterns were acquired from a STOE STADI P diffractometer operating in Debye-Scherrer geometry with monochromated Mo-Kα (λ = 0.70930 Å) radiation and three Mythen 1K strip detectors in stationary mode, covering a 2θ range of 0–55°. Where required, temperature control was achieved by means of an Oxford Cryostreams nitrogen cryostream system.

Simulated patterns were obtained using CrystalDiffract (v7.0.5) utilising a Gaussian peak profile with a peak width of 0.12° (λ = 1.540598 Å) or 0.08° (λ = 0.70930 Å).

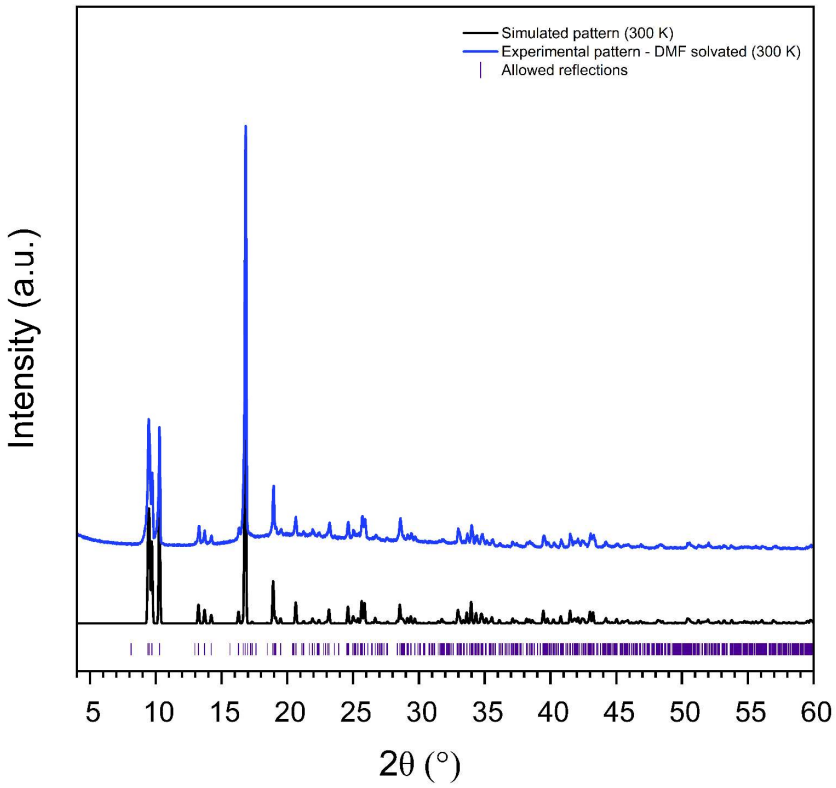

Figure S12 Comparison of PXRD pattern (λ = 1.540598 Å) of as-synthesised **ZnCB-1** (blue) with the PXRD pattern simulated from the single crystal structure obtained at 300 K (black); tick marks (purple) indicate allowed reflections from the obtained SCXRD structure.

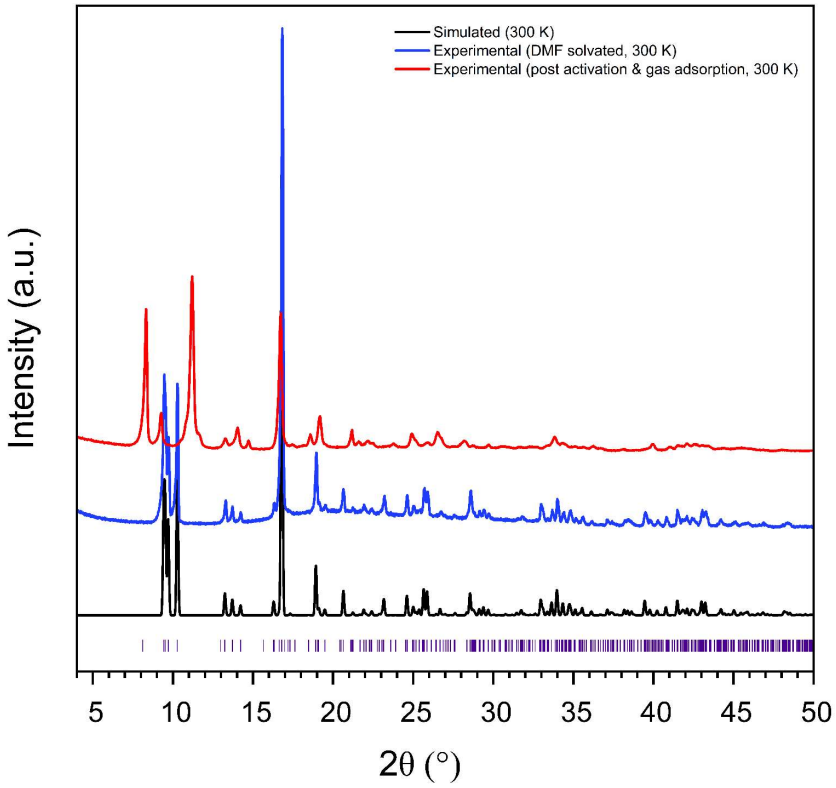

Figure S13 Comparison of PXRD patterns (λ = 1.540598 Å) of the simulated pattern (black), the initially obtained as-synthesised pattern (blue, solvated in DMF), and the sample post activation and gas adsorption experiments (red). Tick marks (purple) indicate allowed reflections from the obtained SCXRD structure for the DMF solvated MOF at 300 K (as unfortunately we were unable to obtain an SCXRD X-ray structure of the desolvated phase, as described earlier). Agreement between the DMF-solvated and activated patterns obtained (with some minor differences at low 2θ) indicates reasonably high stability to thermal activation under vaccuum and retention of long range order. The Bragg reflections of the activated phase are broadly consistent with an orthorhombic cell, $a \approx 19.08$ Å, $b \approx 15.40$ Å, $c \approx 15.67$ Å, where major peak indexing gives Miller indices at 8.33°, 9.28°, 11.28°, and 16.75° of (011), (200), (002), and (022), respectively. Note that as discussed further in the main manuscript, taken together with the SCXRD data, the PXRD results indicate that **ZnCB-1** undergoes a wine-rack-type flexing to a more open form upon activation. Additionally, as demonstrated in **Figure S14**, this change in the PXRD pattern is reversible upon resolvating the desolvated MOF in DMF, further supporting the reversibility of this wine-rack deformation.

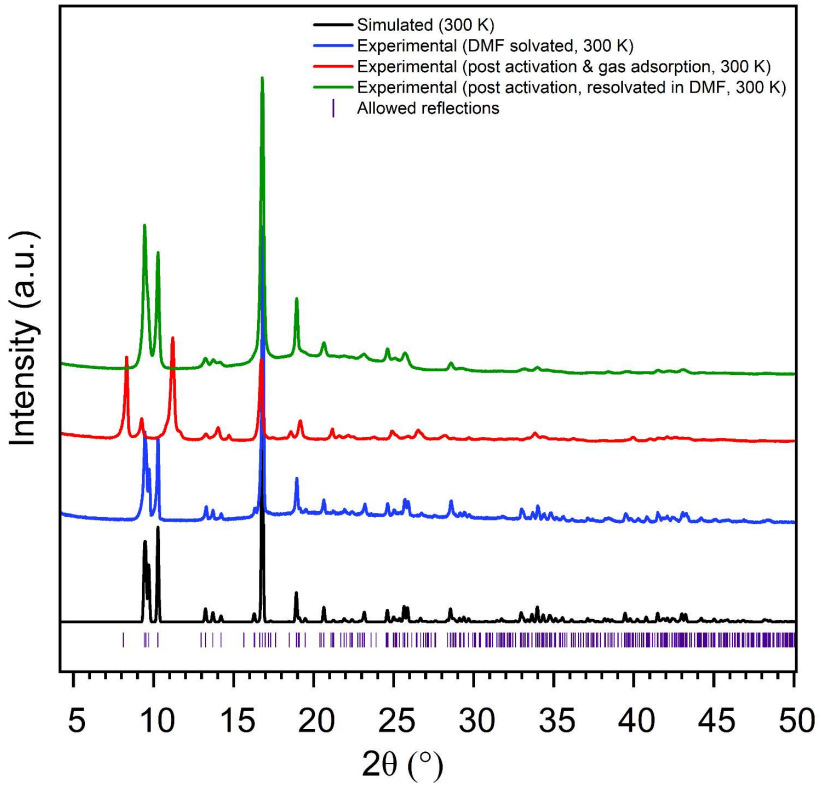

Figure S14 Comparison of PXRD patterns (λ = 1.540598 Å) of the simulated pattern (black), the initially obtained as-synthesised pattern (blue, solvated in DMF), the sample post-activation and gas adsorption experiments (red), and that same post-activation/gas adsorption sample that was then resolvated in DMF (green). Tick marks (purple) indicate allowed reflections from the obtained SCXRD structure for the DMF solvated MOF at 300 K. The changes in the PXRD pattern upon activation are reversed upon resolvating in DMF, indicating that the structural change is indeed reversible (albeit with some broadening of peaks which may be attributable to slight loss of crystallinity and/or the smaller crystallite size upon crystal cracking upon desolvation).

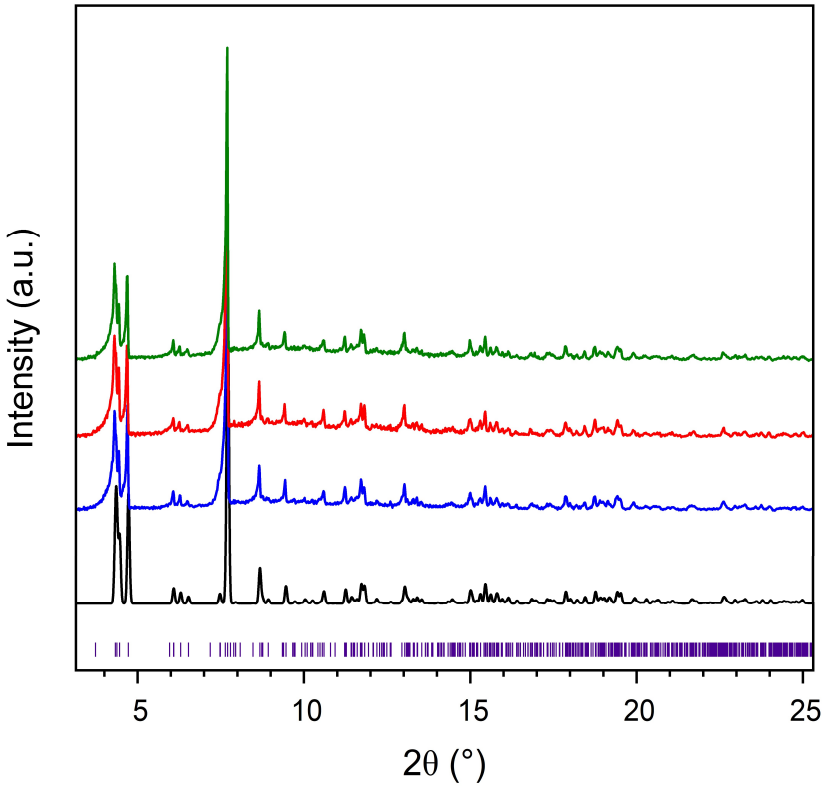

Figure S15 Comparison of PXRD patterns (λ = 0.70930 Å) of three different batches of as-synthesised **ZnCB-1** synthesised in triplicate (simulated = black, Batch 1 = blue, Batch 2 = red, Batch 3 = green), emphasising the high level of repeatability of the MOF synthesis. Tick marks (purple) indicate allowed reflections from the obtained SCXRD structure at 300 K.

S4 – Nuclear Magnetic Resonance (NMR)

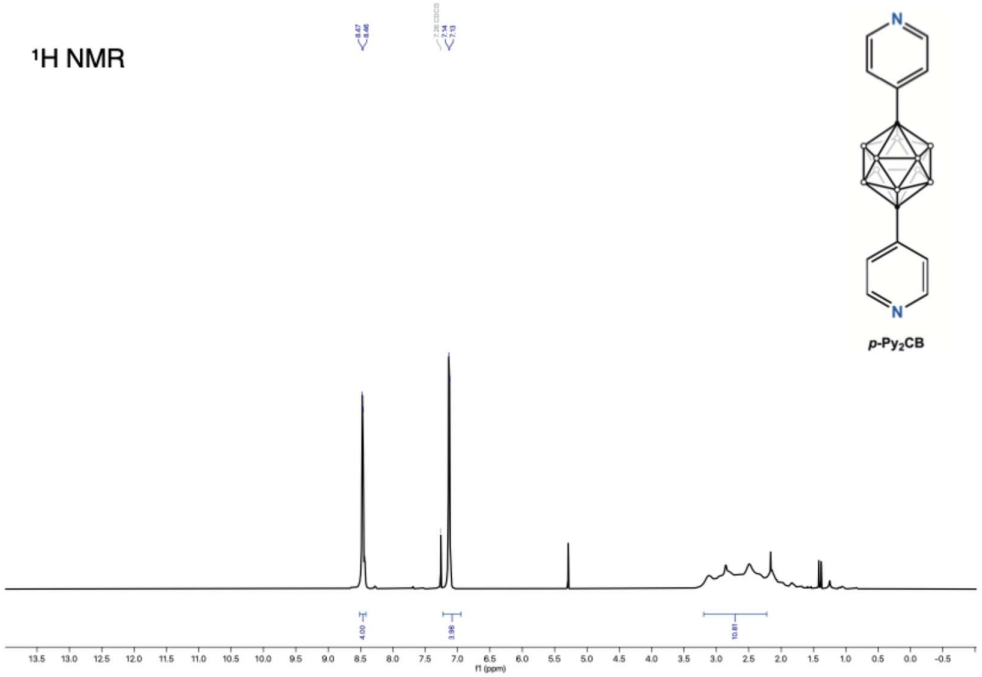

Figure S16 ^{1}H NMR spectrum of *p*-Py_2CB in $CDCl_3$. • (C) and ◦ (BH).

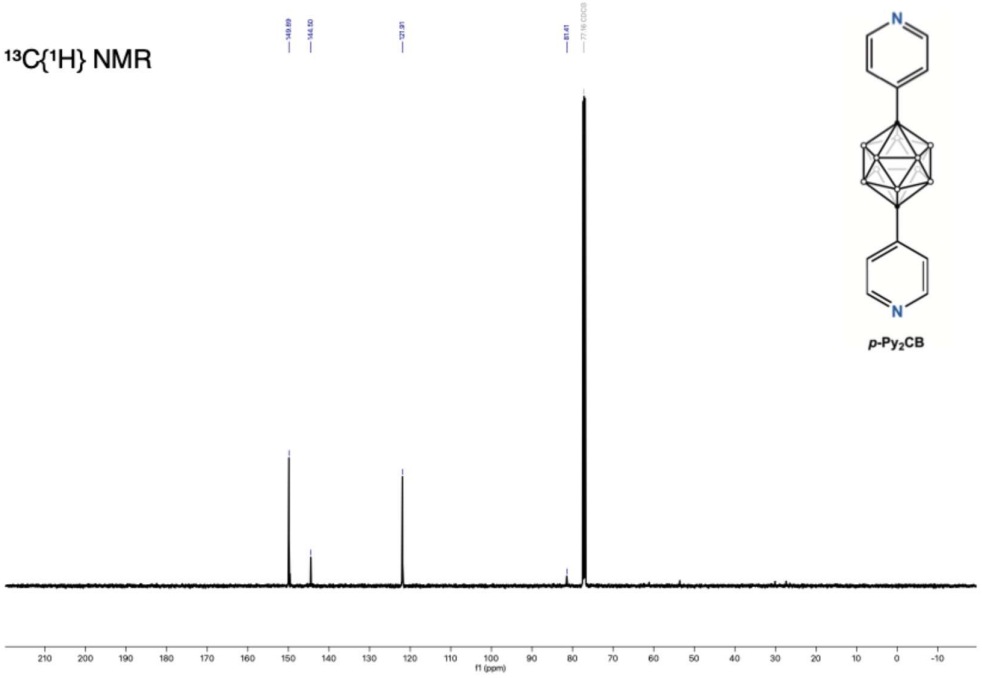

Figure S17 $^{13}C\{^{1}H\}$ NMR spectrum of *p*-Py_2CB in $CDCl_3$. • (C) and ◦ (BH).

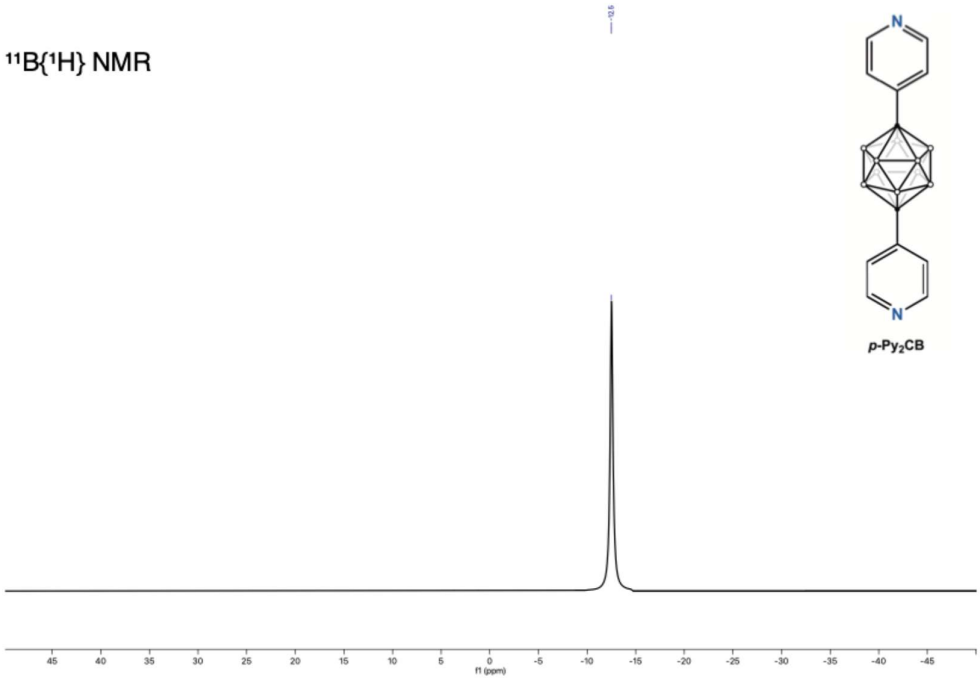

Figure S18 $^{11}B\{^{1}H\}$ NMR spectrum of *p*-Py_2CB in $CDCl_3$. • (C) and ◦ (BH).

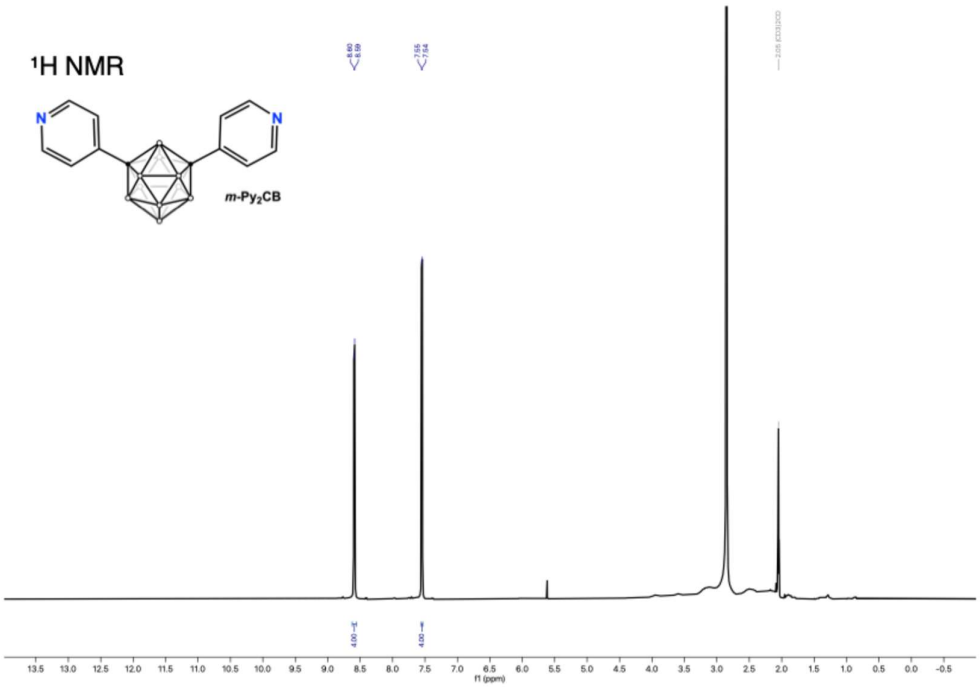

Figure S19 ^{1}H NMR spectrum of *m*-Py_2CB in acetone-d_6. • (C) and ◦ (BH).

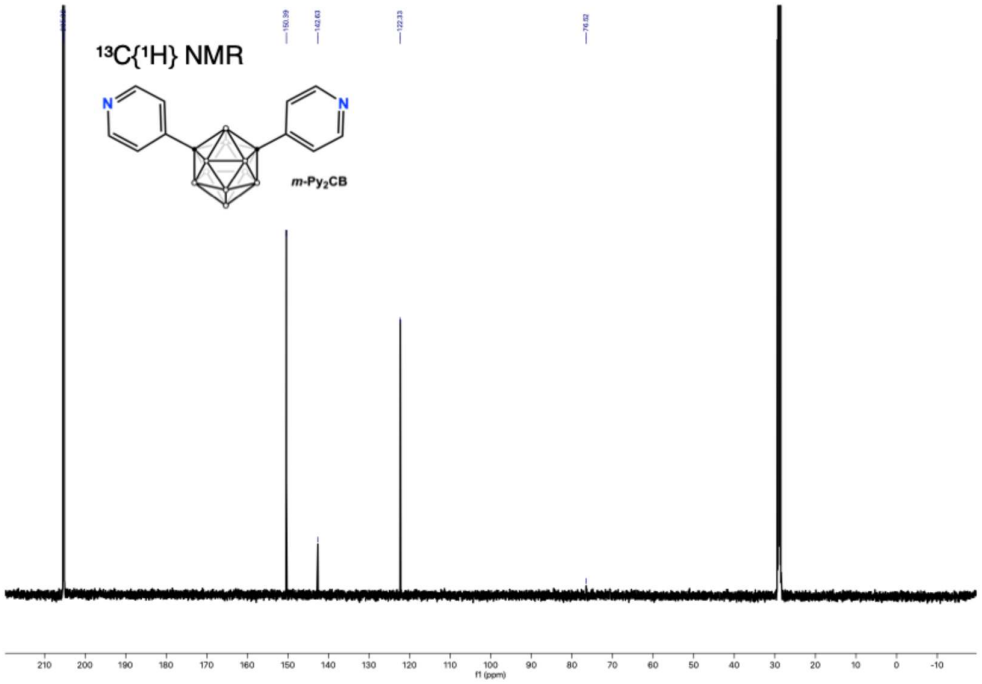

Figure S20 $^{13}C\{^{1}H\}$ NMR spectrum of *m*-Py$_2$CB in acetone-d_6. • (C) and ◦ (BH).

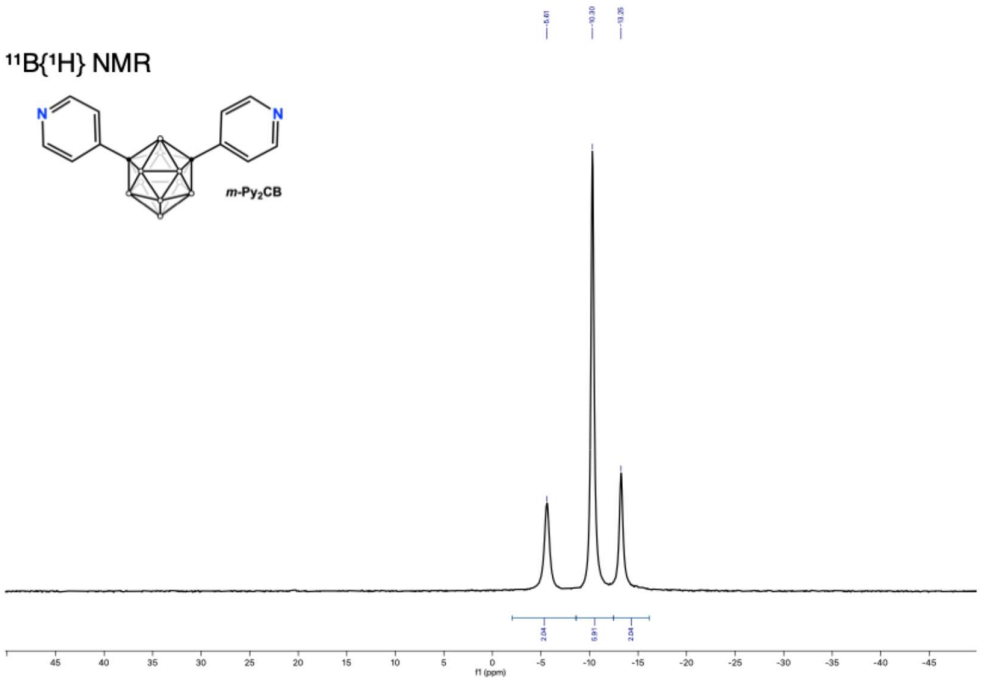

Figure S21 $^{11}B\{^{1}H\}$ NMR spectrum of *m*-Py$_2$CB in acetone-d_6. • (C) and ◦ (BH).

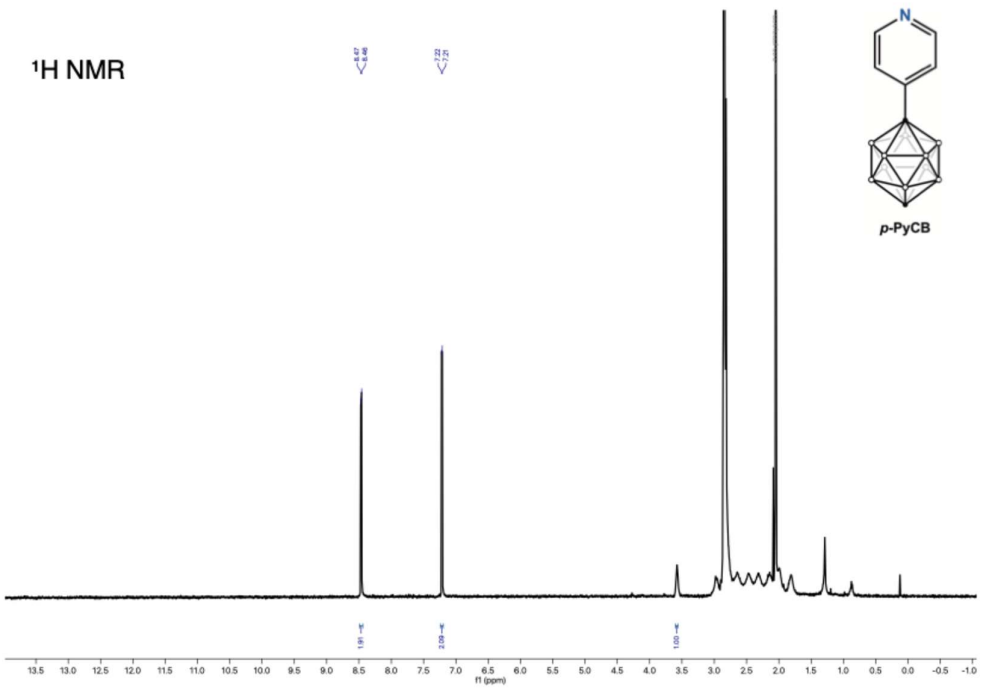

Figure S22 ^{1}H NMR spectrum of *p*-PyCB in acetone-d_6. • (C or CH) and ◦ (BH).

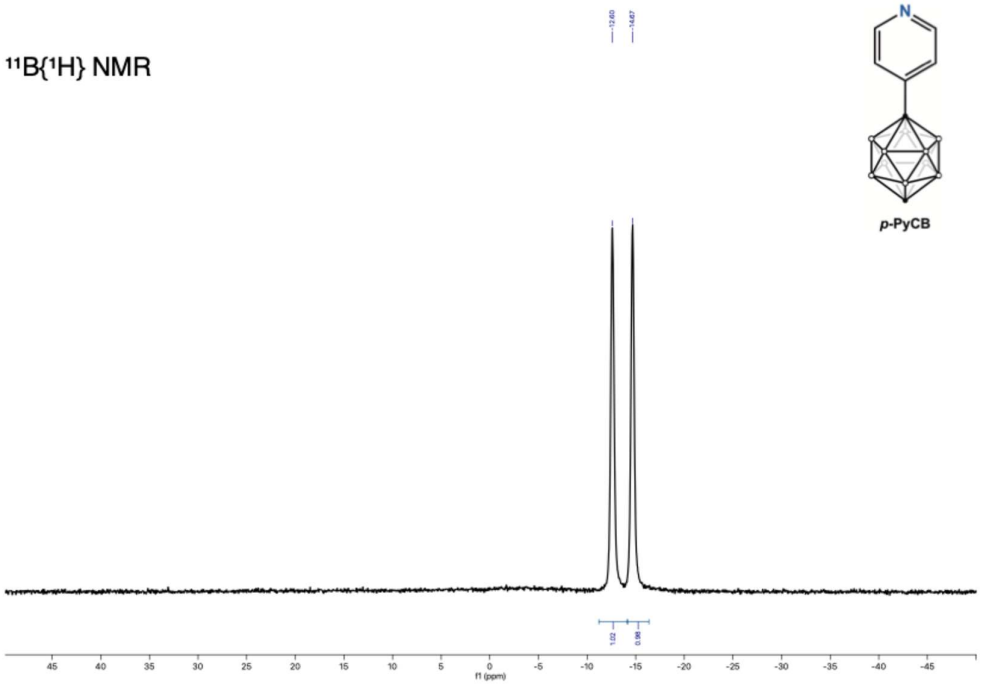

Figure S23 ^{11}B{^{1}H} NMR spectrum of *p*-PyCB in acetone-d_6. • (C or CH) and ◦ (BH).

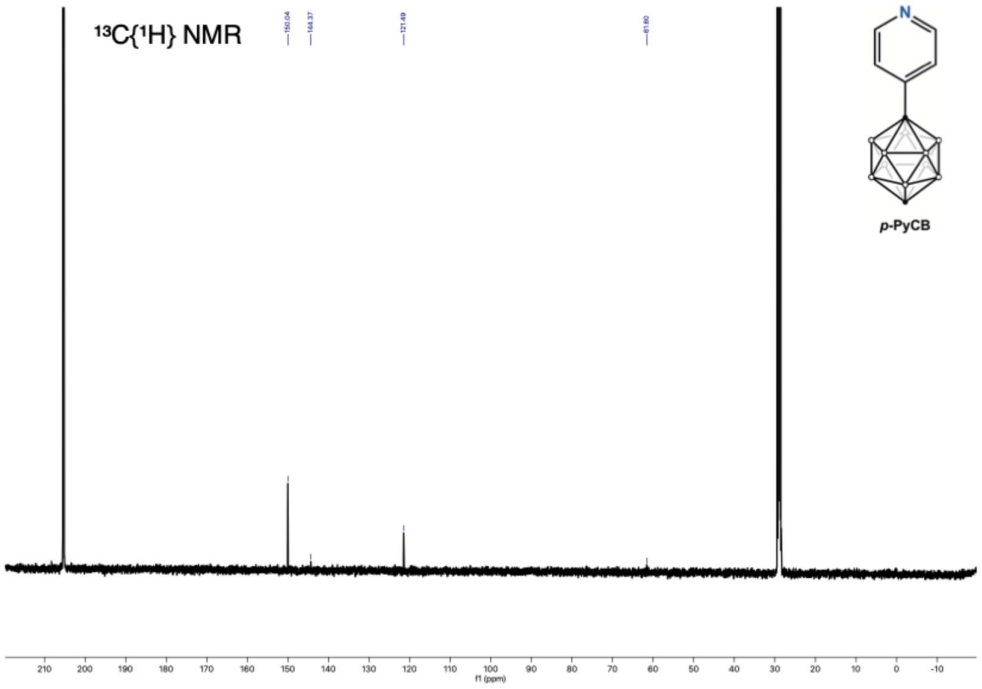

Figure S24 $^{13}C\{^{1}H\}$ NMR spectrum of *p*-PyCB in acetone-d_6. • (C or CH) and ◦ (BH).

S5 – Raman Spectroscopy

Raman scattering spectra were acquired using a Renishaw InVia Qontor confocal spectrometer. Samples were excited using a Renishaw plc RL785 red diode laser outputting an excitation wavelength of 785 nm (5–25% laser power, 40–50 mW) and were referenced internally with respect to silicon at 520.5 ± 0.1 cm^{-1}. Single crystalline samples were loaded onto a Linkam FTIR 600 cryostage fitted with a glass window. A Leica 20× objective was used to focus the laser beam perpendicularly onto the samples. Spectra were recorded on a Renishaw Centrus 2957N7 CCD detector using 10 second exposure times averaged over three accumulations. Data were processed (WiRE 5.0, Renishaw) with baseline subtractions and cosmic ray removal as required.

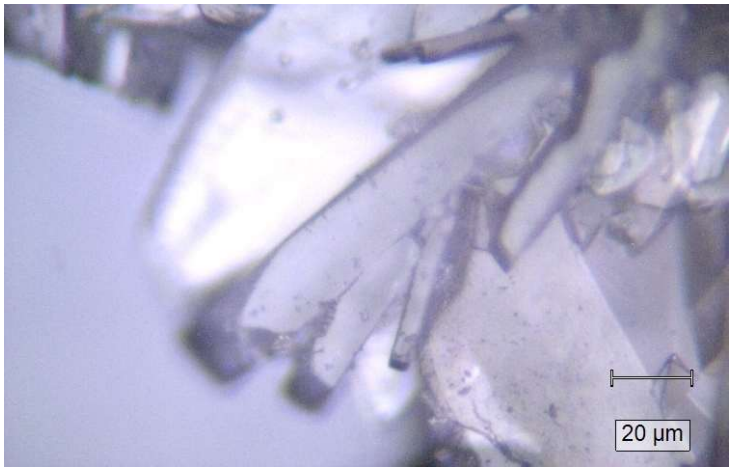

Figure S25 Magnification of *p*-Py_2CB crystals used to acquire Raman spectra.

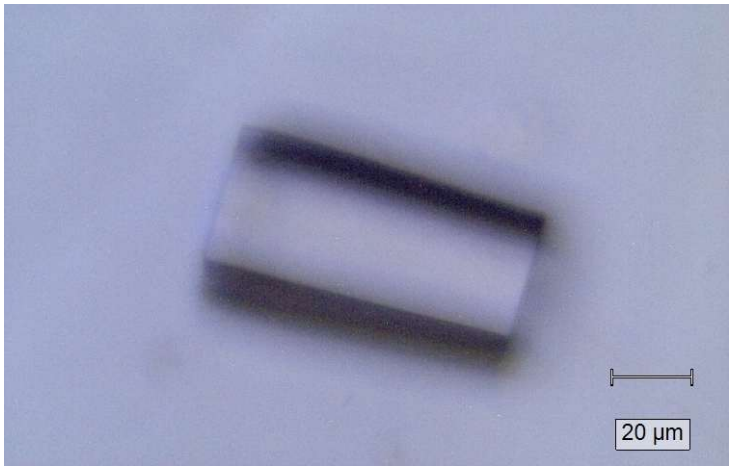

Figure S26 Magnification of **ZnCB-1** single crystal used to acquire Raman spectra.

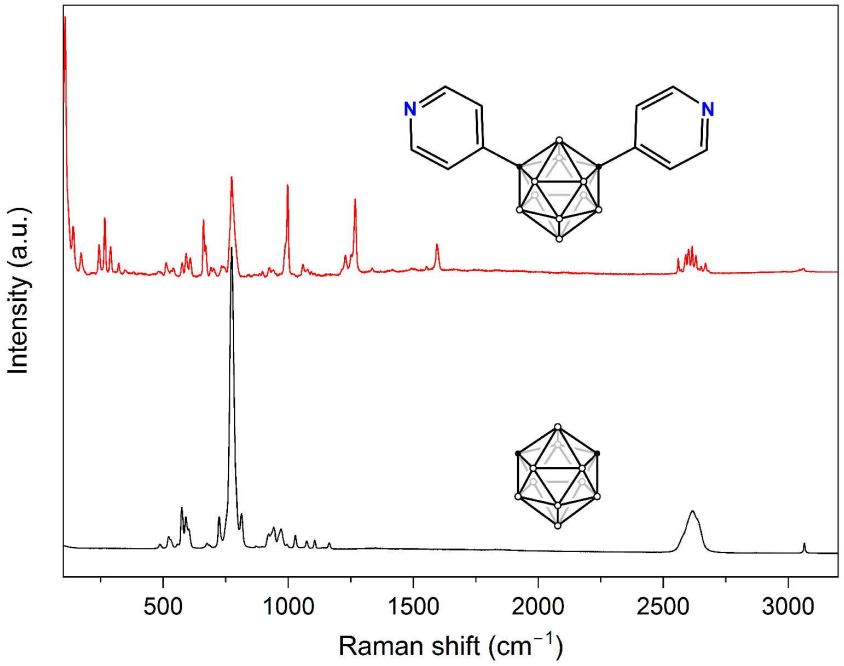

Figure S27 Raman spectra of *m*-CB (black) and *m*-Py_2CB (red) acquired using 785 nm excitation at 10 s exposure times and averaged over three accumulations. • (C or CH), ◦ (BH).

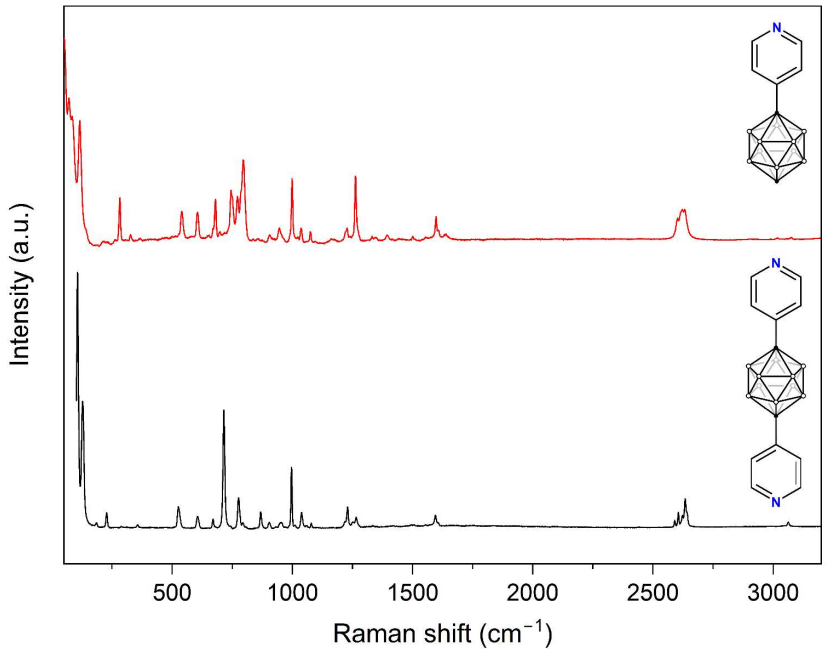

Figure S28 Raman spectra of *p*-Py_2CB (black) and *p*-PyCB (red) acquired using 785 nm excitation at 10 s exposure times and averaged over three accumulations. • (C or CH), ◦ (BH).

S6 – Mass Spectrometry

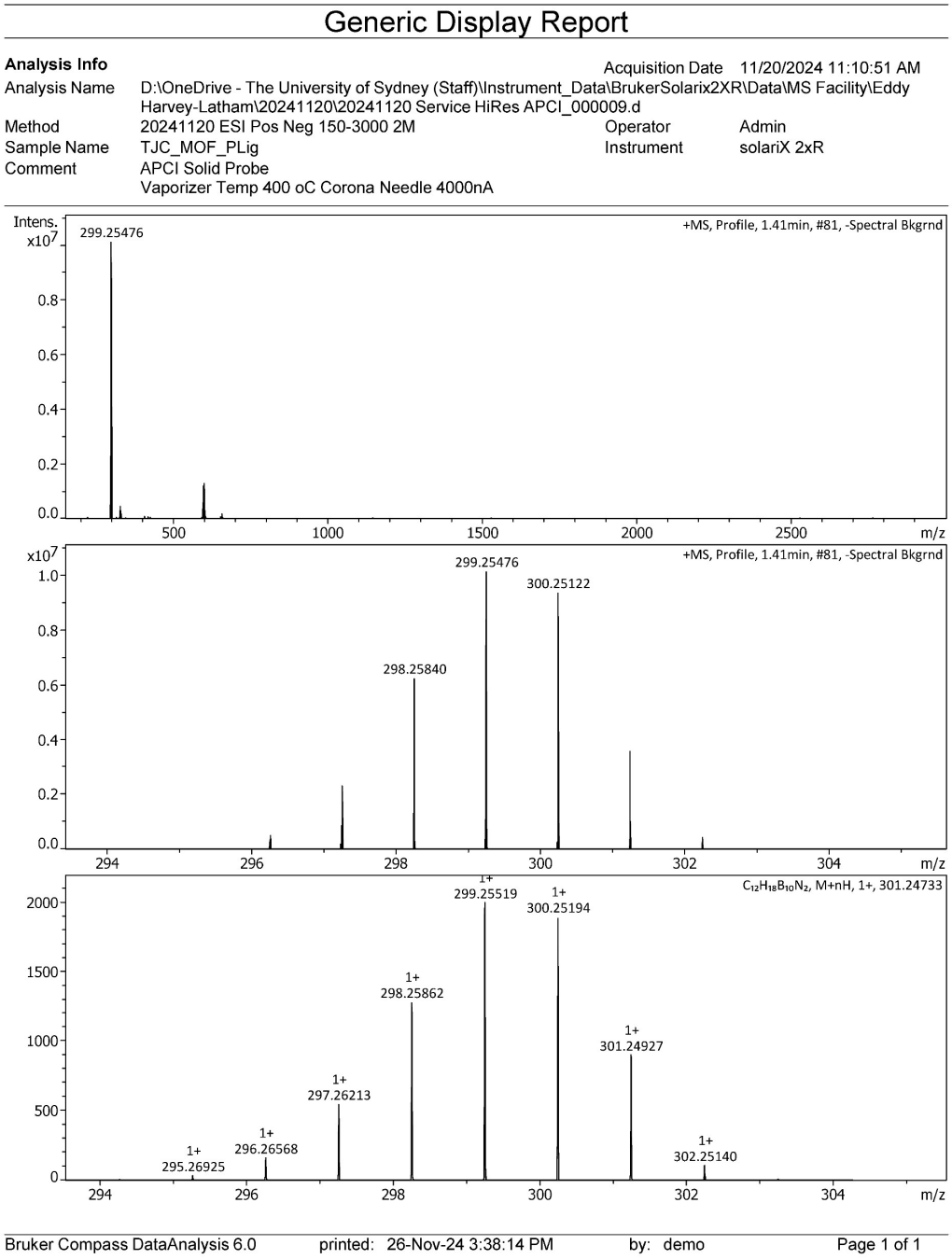

Figure S29 APCI-HRMS of *p*-Py_2CB.

Generic Display Report

Analysis Info Acquisition Date 11/20/2024 10:24:11 AM

Analysis Name	D:\OneDrive - The University of Sydney (Staff)\Instrument_Data\BrukerSolarix2XR\Data\MS Facility\Eddy Harvey-Latham\20241120\20241120 Service HiRes APCI_000001.d		
Method	20241120 ESI Pos Neg 150-3000 2M	Operator	Admin
Sample Name	TJC-MOF-MLig	Instrument	solariX 2xR
Comment	APCI Solid Probe Vaporizer Temp 400 oC Corona Needle 4000nA		

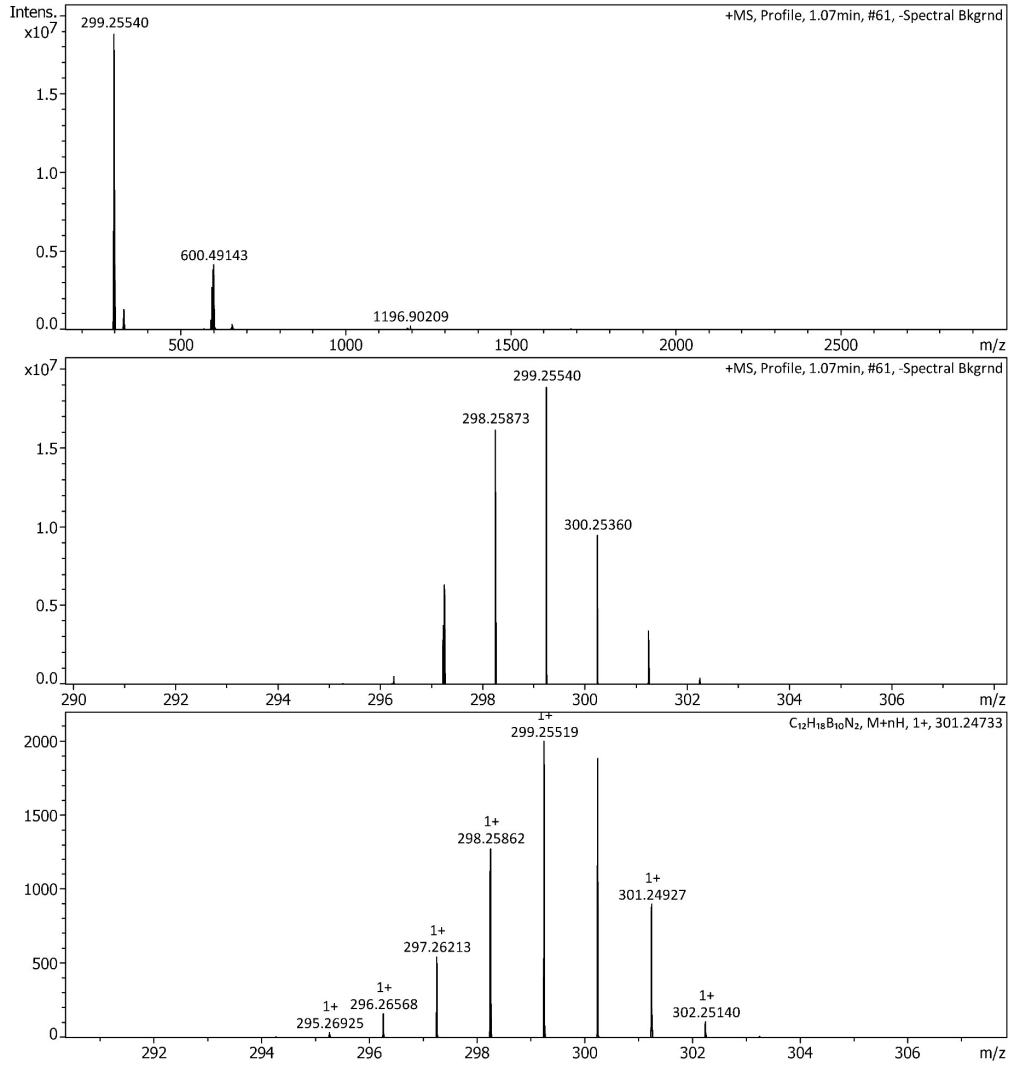

Bruker Compass DataAnalysis 6.0 printed: 26-Nov-24 3:23:12 PM by: demo Page 1 of 1

Figure S30 APCI-HRMS of *m*-Py_2CB.

Generic Display Report

Analysis Info

		Acquisition Date	11/20/2024 11:00:38 AM
Analysis Name	D:\OneDrive - The University of Sydney (Staff)\Instrument_Data\BrukerSolarix2XR\Data\MS Facility\Eddy Harvey-Latham\20241120\20241120 Service HiRes APCI_000008.d		
Method	20241120 ESI Pos Neg 150-3000 2M	Operator	Admin
Sample Name	TJC-MOF-Pligmono	Instrument	solariX 2xR
Comment	APCI Solid Probe Vaporizer Temp 400 oC Corona Needle 4000nA		

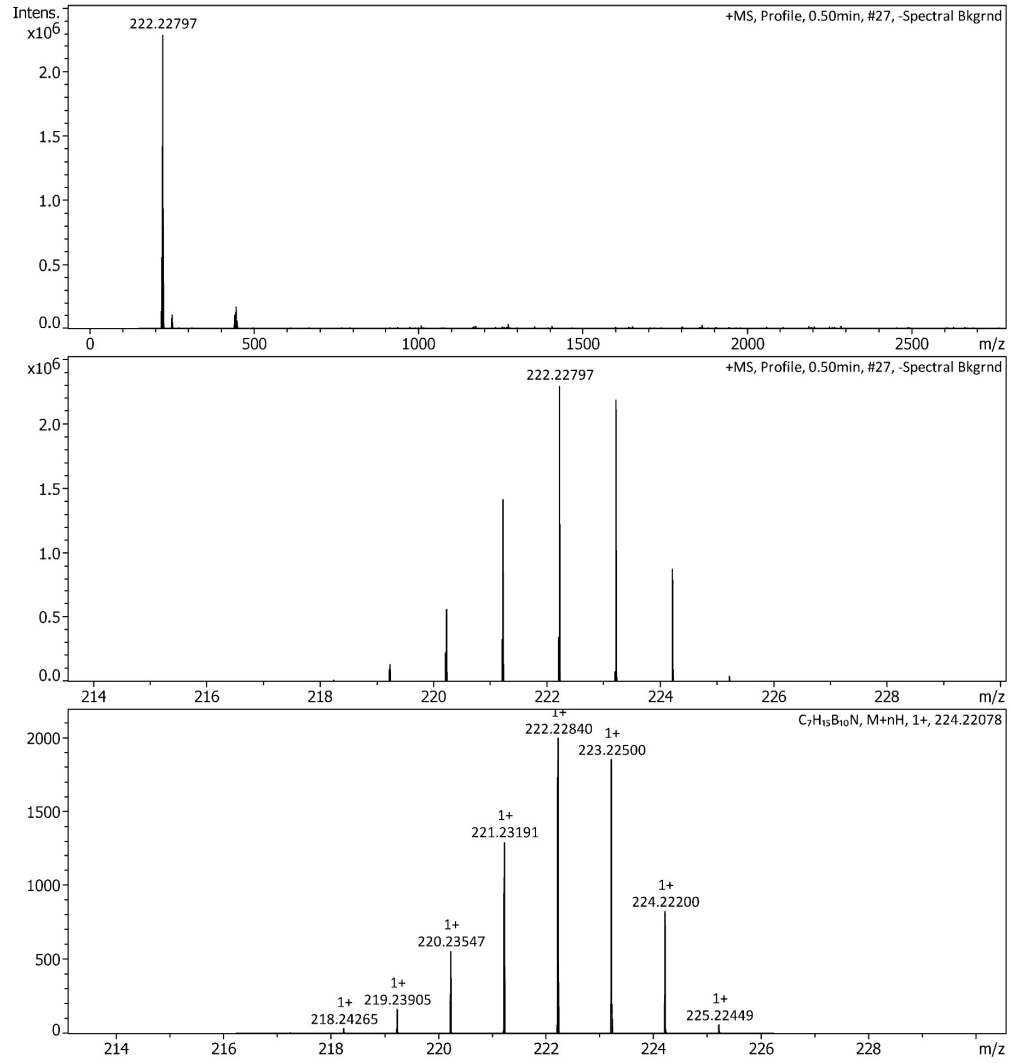

Bruker Compass DataAnalysis 6.0 printed: 26-Nov-24 3:29:08 PM by: demo Page 1 of 1

Figure S31 APCI-HRMS of *p*-PyCB.

S7 – Thermogravimetric Analysis (TGA)

TGA data were acquired from a TA Instruments Discovery TGA Thermogravimetric Analyser. Samples (*ca.* 10 mg) were first washed several times with DMF to remove any residual unreacted starting material and were then briefly dried under a stream of nitrogen gas before being loaded onto a pre-tared Pt pan sample holder. Samples were then isothermally heated at 30 °C for 10 minutes and under a constant stream of dry nitrogen with a flow rate of 20 mL min^{-1}. A temperature ramping step was conducted at a rate of 5 °C min^{-1} to a final temperature of 650 °C.

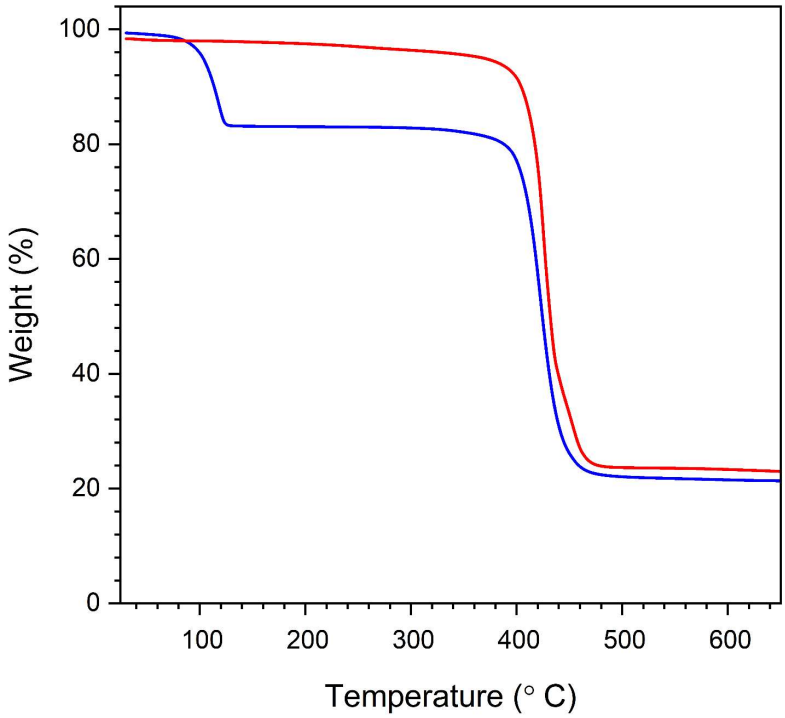

Figure S32 TGA traces of **ZnCB-1** as as-synthesised (blue) and post-activation samples (red) (i.e., following gas adsorption experiments described below) over the temperature range 30–650 °C. Note that the 17% weight loss observed between 100–120 °C aligns closely with the hypothetical weight loss of 1 molecule of DMF per formula unit. The formula unit of the solvated MOF is: $C_{14}H_{13}B_5NO_4Zn,C_3H_7NO$ (M_W = 451.80 g mol^{-1}), and the anticipated guest-free framework would be $C_{14}H_{13}B_5NO_4Zn$ (M_W = 378.70 g mol^{-1}). Therefore the estimated mass loss would be 1 − (378.70/451.80) = 16.2%.

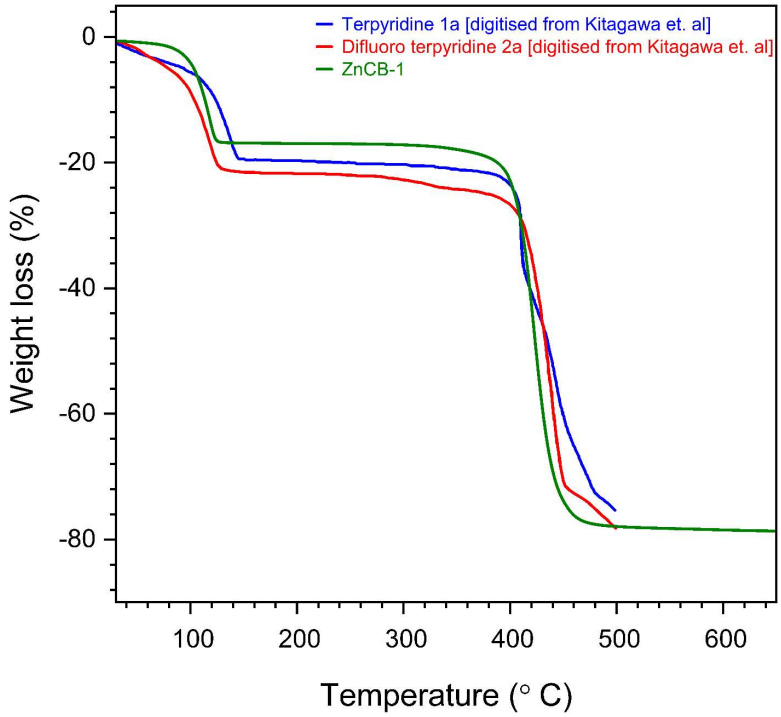

Figure S33 Comparison between TGA traces of **ZnCB-1** (green) and MOFs **1a** (blue) and **2a** (red) reported by Kitagawa *et al.*[5] Plots were digitised using the PlotDigitizer Pro App.

S8 – Gas Adsorption

Gas adsorption isotherms were collected on **ZnCB-1** following solvent exchange of the crystals from DMF to DCM (washed 3 × 10 mL with DMF, then solvent exchanged with DCM with 5 × replenishments over the course of two days). The N_2 adsorption isotherm of **ZnCB-1** at 77 K exhibited essentially negligible uptake which indicates that the activated MOF was non-porous to nitrogen at this temperature (Fig. 3(c), manuscript). To further probe the adsorption properties of **ZnCB-1**, CO_2 adsorption isotherms were collected at three different temperatures as it is well known that CO_2 can penetrate pores that are inaccessible to nitrogen as a result of its increased polarity, reduced kinetic diameter (3.30 Å for CO_2 compared with 3.64 Å for N_2), and the relatively higher temperature of the corresponding experiments, all of which contribute to faster diffusion, particularly in ultramicroporous materials with pores of < 7 Å, as is the case with **ZnCB-1**.[6]

As shown in the main manuscript (Fig. 3(c)), the maximal CO_2 uptake (at ~1 bar) was 62.4 cm^3 g^{-1}, 21.0 cm^3 g^{-1}, and 12.6 cm^3 g^{-1} for the 195 K, 273 K, and 293 K isotherms, respectively. All isotherms exhibited reversible behaviour with no significant evidence of hysteresis. As expected, increasing the temperature of the gas adsorption experiment results in a decrease in the maximal amount of CO_2 adsorbed. The amount of adsorbed CO_2 at 195 K approaches a saturation value of 62.4 cm^3/g (2.79 mmol/g, 12.26 wt %) at ~ 960 mbar, which corresponds to approximately 1.06 molecules of CO_2 per Zn^{2+} ion in the framework.

The negligible uptake of N_2 is consistent with the pore analysis performed using the Mercury Pore Analyzer function (on the 300 K obtained CIF, and with no disorder modelled or solvents included), which indicates a pore limiting diameter of 3.58 Å (i.e., smaller than the kinetic diameter of N_2 guests) and a maximum pore diameter of 4.22 Å.

The pore-size distribution was calculated from the 195 K CO_2 isotherms employing the Horvath–Kawazoe (HK) method (as implemented in Micromeritics Flex V6.0 software), with pores between 3.42–5.19 Å (median pore size is 4.41 Å), which is generally consistent with the values calculated from the above Mercury analysis of the SCXRD data, which suggested pores between 3.58–4.22 Å (see Figs. S34–35). The maximum cumulative pore volume estimated from the HK method was 0.097 cm^3/g.

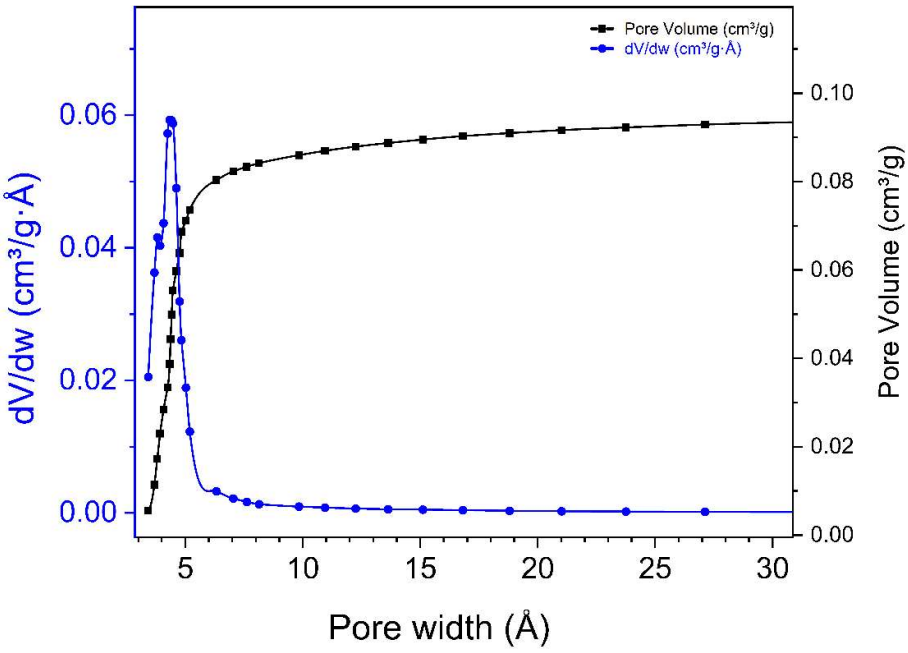

Figure S34 Pore size distribution and cumulative pore volume for **ZnCB-1** derived from the 195 K CO_2 isotherm employing the Horvath–Kawazoe (HK) method.

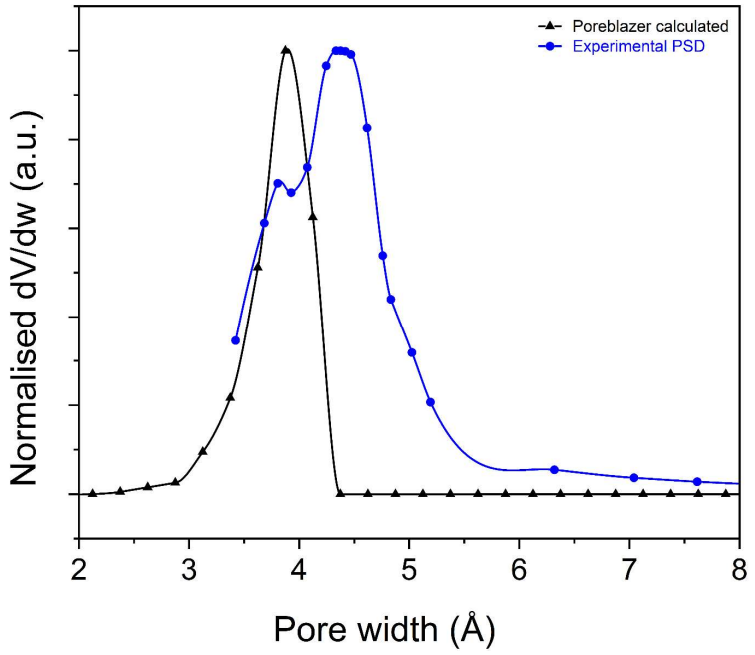

Figure S35 Pore size distribution as calculated from the disorder-free and solvent-free 300 K CIF utilising PoreBlazer v4.0[7] (with default paramaters) (black) and experimental pore size distribution for **ZnCB-1** derived from the 195 K CO_2 isotherm employing the HK method (blue). In general, the experimental PSD suggests slightly larger pores in the desolvated phase than those calculated from the obtained CIF, which is consistent with the unit cell changes/wine-rack deformation suggested from the PXRD data (discussed further above).

Virial Fits – Enthalpy of Adsorption

Virial analysis was undertaken by fitting the 273 K and 293 K isotherms *via* global optimisation to the virial equation to determine the heat of adsorption (Q_{st}) as a function of CO_2 loading, which was then converted to the isosteric enthalpy of adsorption (i.e. $\Delta H_{ads} = -Q_{st}$) as recommended.[8]

The virial fit is based on the exponential virial equation which is most commonly published as:[8]

$$\ln p = \ln n + \frac{1}{T}\sum_{i=0}^{m} a_i n^i + \sum_{i=0}^{m} b_i n^i \qquad (1)$$

Where p is pressure (kPa), n is the amount of gas adsorbed (mmol/g), T is the temperature in K (e.g. 273 K or 293 K) a_i and b_i are the virial coefficients, and m represents the number of coefficients required to appropriately fit the isotherms.

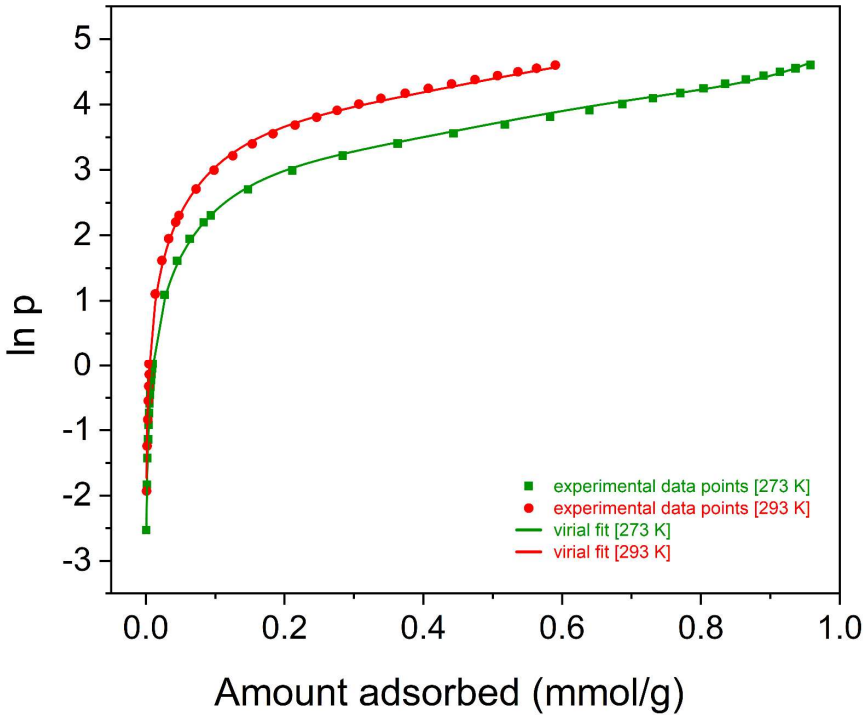

Figure S36 Experimental CO_2 adsorption data for **ZnCB-1** at 273 K (green squares) and 293 K (red circles) with corresponding virial fits obtained through global optimisation (green and red lines, respectively).

Table S5 Virial fitting parameters obtained from global optimisation fitting of the two CO_2 adsorption isotherms to the virial equation (Equation 1).

Parameter	Value
a_0	-2700.88 ± 70.58
a_1	806.07 ± 177.1
a_2	-6386.64 ± 1435.12
a_3	16137.08 ± 4234.74
a_4	-17301.28 ± 5174.95
a_5	6825.37 ± 2227.77
b_0	14.46 ± 0.25
R^2	0.99912
Chi^2	0.00413

The heat of adsorption (Q_{st}), which is a function of uptake (n), is then given as:

$$Q_{st}(n) = -R \cdot \sum_{i=0}^{m} a_i \, n^i \tag{2}$$

The heat of adsorption at low uptake/coverage, Q_{st}^0, is then approximated as:

$$Q_{st}^0(n) = -R \cdot a_0 \tag{3}$$

Note that as outlined by Nuhnen *et al.*, the quantity *isosteric* enthalpy of adsorption, ΔH_{ads}, is more meaningful than the simple *heat*, Q. Both magnitudes are equal with opposite sign:

$$\Delta H_{ads} = -Q_{st} \tag{4}$$

From the virial analysis, the isosteric enthalpy of adsorption at very low loadings (ΔH_{ads}^0) was calculated to be −22.45 kJ mol^{-1}, which remained relatively constant up to the maximally recorded loading (across both temperatures) of 0.6 mmol g^{-1} (Figure 3(d), manuscript). Note that this isosteric enthalpy of adsorption at low coverage is consistent with other ultramicroporous MOFs that do not bear any strong adsorption sites such as open metal sites.[9]

BET area determination

The apparent BET area of **ZnCB-1** was estimated from the CO_2 adsorption isotherm collected at 195 K using the BETSI software package, resulting in an apparent BET area of 271 $m^2\ g^{-1}$.[10] Note that studies in the literature have shown that BET areas calculated from CO_2 isotherms collected at 195 K are significantly underestimated compared to those calculated from nitrogen isotherms, and therefore this BET area can be considered as the lower limit of accessible surface area.[6] However, due to the lack of nitrogen uptake at 77 K preventing the estimation of BET area, this is nonetheless a useful value.

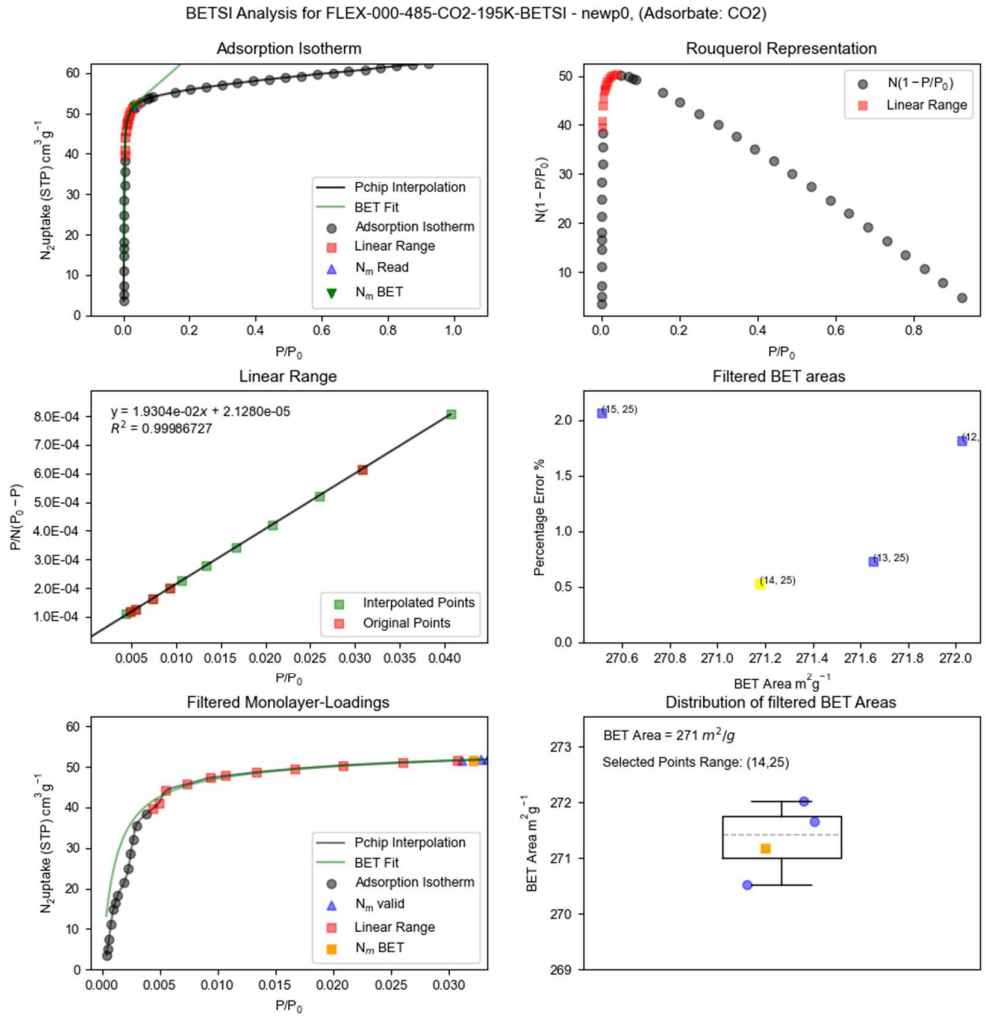

Figure S37 BETSI fitting and apparent BET area calculated for **ZnCB-1** utilising the CO_2 isotherm collected at 195 K.

S9 – Scanning Electron Microscopy (SEM)

SEM micrographs were obtained using a Thermo Scientific Phenom XL Desktop SEM. Prior to SEM measurements, samples were first deposited on conductive carbon tape and then covered with a thin layer (~ 5–10 nm) of gold utilising a Safematic brand CCU-010 Compact Coating Unit. SEM micrographs for imaging were obtained using the Secondary Electron Detector (SED) with an accelerating voltage of 5 kV. Electron Dispersive Spectroscopy (EDS) results were obtained using the backscattered electron detector (BSD) with an accelerating voltage of 15 kV.

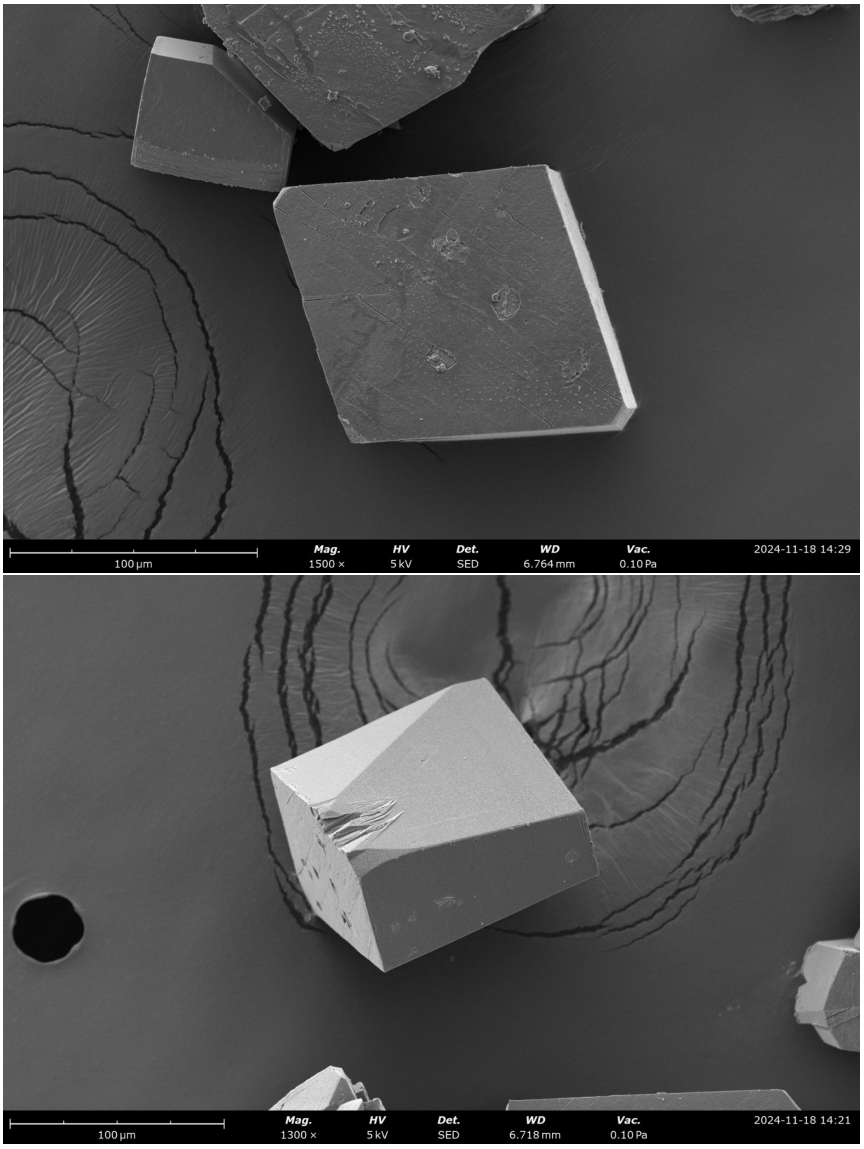

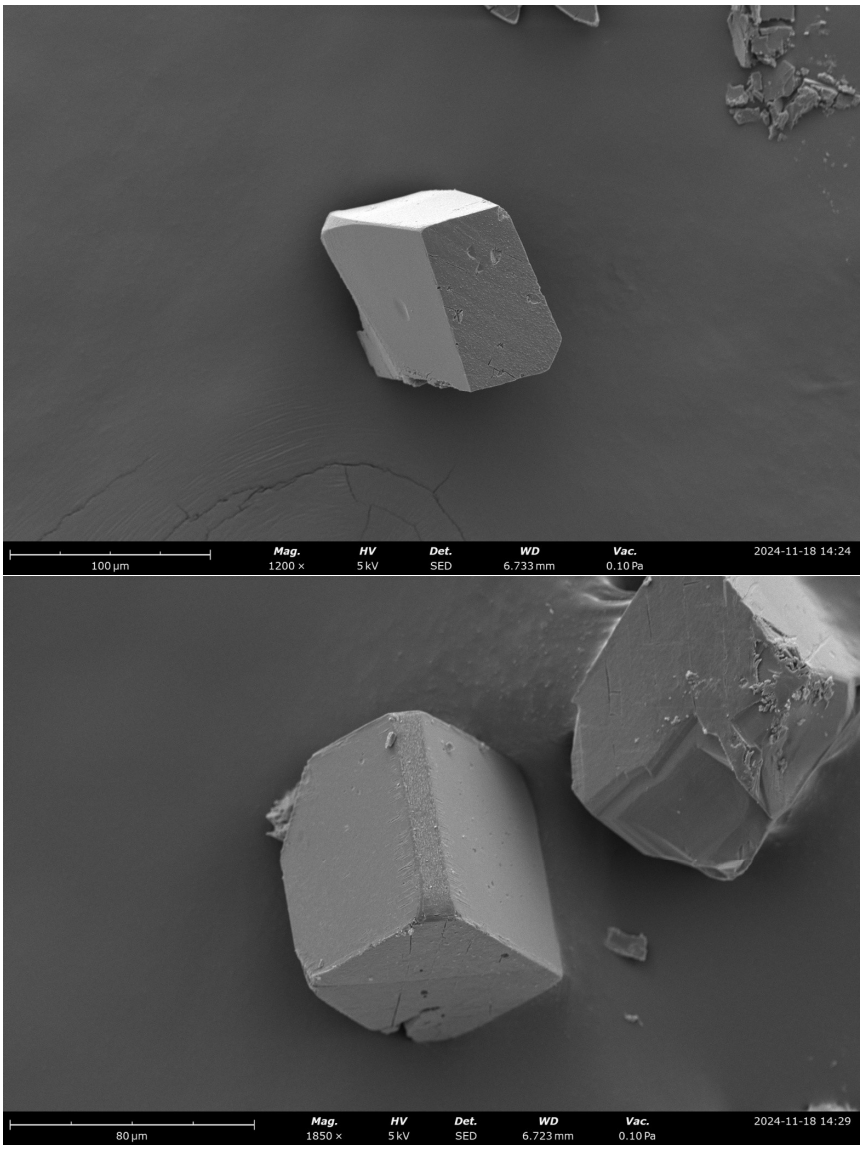

Figure S38 SEM micrographs of representative crystals of **ZnCB-1**.

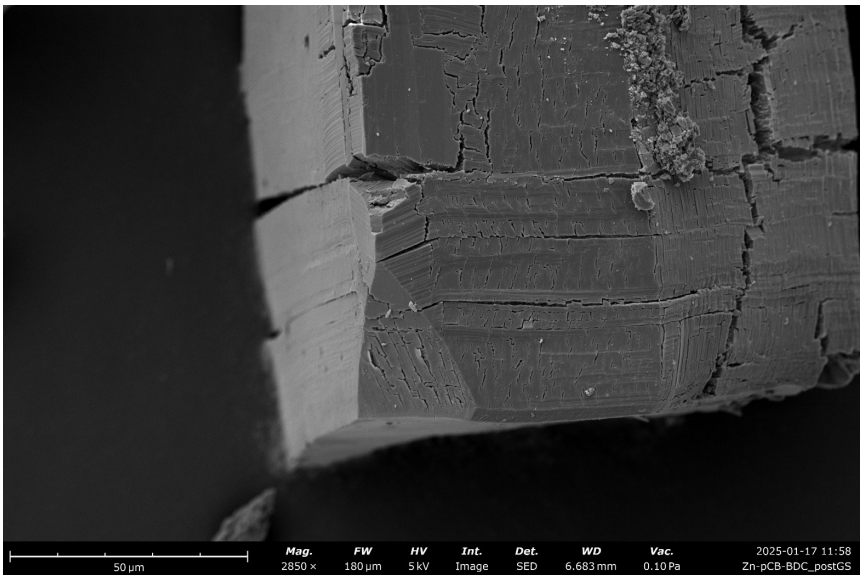

Figure S39 SEM micrograph of **ZnCB-1** crystal post-activation and gas adsorption experiments. As discussed in the manuscript and shown in Figure S5, during attempts to obtain an X-ray structure of the desolvated phase, the **ZnCB-1** crystals were observed to experience a loss of monocrystallinity upon activation. This observation is consistent with the SEM images of the crystals post-activation which exhibited significant cracking, likely due to a change in symmetry and build-up of internal stresses associated with a wine-rack flexing.

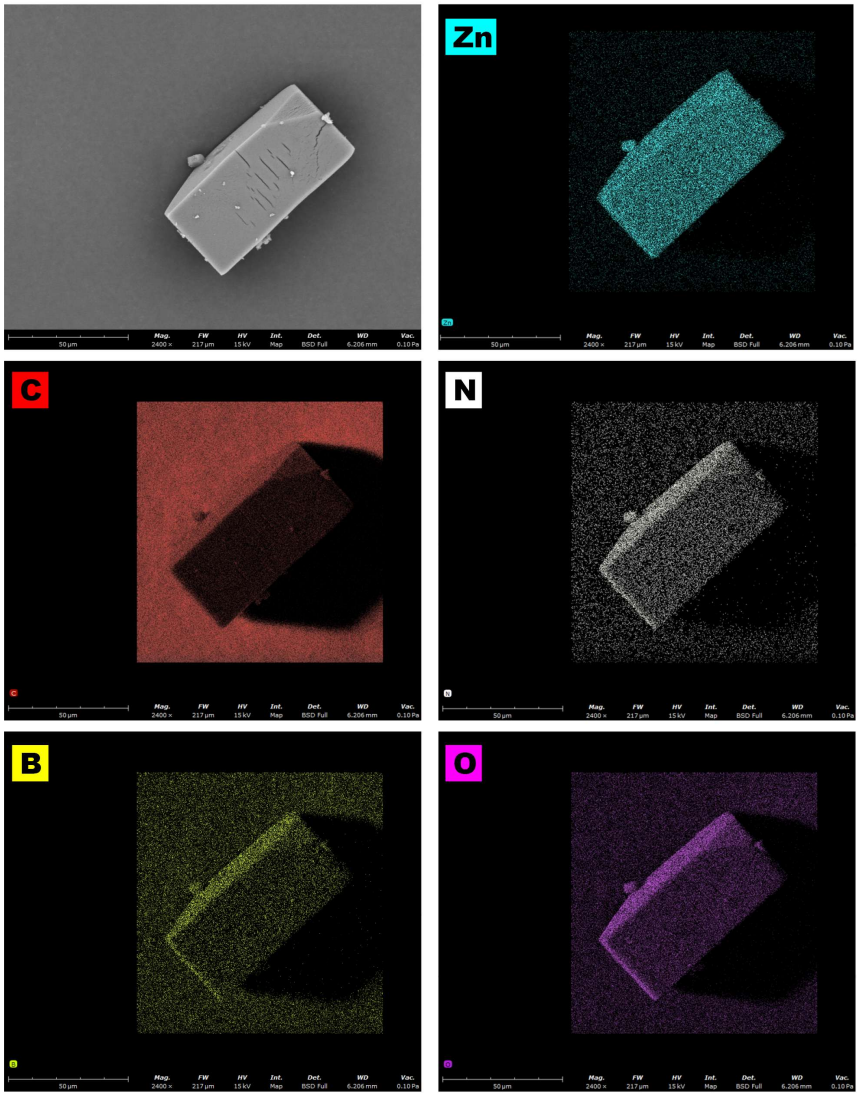

Figure S40 EDS mapping of representative **ZnCB-1** crystal (note adhered to conductive carbon tape) showing a homogeneous distribution of component elements C, B, N, O, and Zn.

S10 – References

1. C. Wolf, G. E. Tumambac and C. N. Villalobos, *Synlett*, 2003, 1801–1804.
2. G. M. Sheldrick, *Acta Crystallogr. Sect. A*, 2015, **71**, 3–8.
3. G. M. Sheldrick, *Acta Crystallogr. Sect. C Struct. Chem.*, 2015, **71**, 3–8.
4. O. V. Dolomanov, L. J. Bourhis, R. J. Gildea, J. A. K. Howard and H. Puschmann, *J. Appl. Cryst.*, 2009, **42**, 339–341.
5. J. Seo, C. Bonneau, R. Matsuda, M. Takata and S. Kitagawa, *J. Am. Chem. Soc.*, 2011, **133**, 9005–9013.
6. T. Islamoglu, K. B. Idrees, F. A. Son, Z. Chen, S.-J. Lee, P. Li and O. K. Farha, *J. Mater. Chem. A*, 2022, **10**, 157–173.
7. L. Sarkisov, R. Bueno-Perez, M. Sutharson and D. Fairen-Jimenez, *Chem. Mater.*, 2020, **32**, 9849–9867.
8. A. Nuhnen and C. Janiak, *Dalton Trans.*, 2020, **49**, 10295–10307.
9. A. Lancheros, S. Goswami, M. R. Mian, X. Zhang, X. Zarate, E. Schott, O. K. Farha and J. T. Hupp, *Dalton Trans.*, 2021, **50**, 2880–2890.
10. J. W. M. Osterrieth, J. Rampersad, D. Madden, N. Rampal, L. Skoric, B. Connolly, M. D. Allendorf, V. Stavila, J. L. Snider, R. Ameloot, J. Marreiros, C. Ania, D. Azevedo, E. Vilarrasa-Garcia, B. F. Santos, X.-H. Bu, Z. Chang, H. Bunzen, N. R. Champness, S. L. Griffin, B. Chen, R.-B. Lin, B. Coasne, S. Cohen, J. C. Moreton, Y. J. Colón, L. Chen, R. Clowes, F.-X. Coudert, Y. Cui, B. Hou, D. M. D'Alessandro, P. W. Doheny, M. Dincă, C. Sun, C. Doonan, M. T. Huxley, J. D. Evans, P. Falcaro, R. Ricco, O. Farha, K. B. Idrees, T. Islamoglu, P. Feng, H. Yang, R. S. Forgan, D. Bara, S. Furukawa, E. Sanchez, J. Gascon, S. Telalović, S. K. Ghosh, S. Mukherjee, M. R. Hill, M. M. Sadiq, P. Horcajada, P. Salcedo-Abraira, K. Kaneko, R. Kukobat, J. Kenvin, S. Keskin, S. Kitagawa, K. I. Otake, R. P. Lively, S. J. A. DeWitt, P. Llewellyn, B. V. Lotsch, S. T. Emmerling, A. M. Pütz, C. Martí-Gastaldo, N. M. Padial, J. García-Martínez, N. Linares, D. Maspoch, J. A. Suárez del Pino, P. Moghadam, R. Oktavian, R. E. Morris, P. S. Wheatley, J. Navarro, C. Petit, D. Danaci, M. J. Rosseinsky, A. P. Katsoulidis, M. Schröder, X. Han, S. Yang, C. Serre, G. Mouchaham, D. S. Sholl, R. Thyagarajan, D. Siderius, R. Q. Snurr, R. B. Goncalves, S. Telfer, S. J. Lee, V. P. Ting, J. L. Rowlandson, T. Uemura, T. Iiyuka, M. A. van der Veen, D. Rega, V. Van Speybroeck, S. M. J. Rogge, A. Lamaire, K. S. Walton, L. W. Bingel, S. Wuttke, J. Andreo, O. Yaghi, B. Zhang, C. T. Yavuz, T. S. Nguyen, F. Zamora, C. Montoro, H. Zhou, A. Kirchon and D. Fairen-Jimenez, *Adv. Mater.*, 2022, **34**, e2201502.